$Co_4(PW_9O_{34})_2$ Polyoxmetalate Cluster Intercalated in Layered Double Hydroxides as Catalyst for the Oxidation of *p*-Arsanilic Acid and Subsequent Immobilization of Arsenic-Containing Byproducts

Hanxuan Zeng[a], Wenfang Shi[a], Bufan Yang[a], Jing Deng[a], Jue Wang[b,*], Haojie Zhang[c]

a. College of Civil Engineering, Zhejiang University of Technology, Hangzhou, 310023, P.R. China

b. College of Architecture and Energy Engineering, Wenzhou University of Technology, Wenzhou, 325000, P.R. China

c. Department of Environmental Engineering, Helmholtz Centre for Environmental Research-UFZ, Leipzig, 04318, Germany

*Corresponding author.

E-mail address: wangjue0119@hnu.edu.cn (J. Wang).

Abstract

The ecological risk associated with the hidden release of inorganic arsenic from *p*-arsanilic acid (*p*-ASA) due to microbial activities and sunlight irradiation underscores the urgent need for an effective *p*-ASA control strategy. Herein, polyoxometalate clusters intercalated layered double hydroxides (LDH-CoPW) were synthesized to activate peroxymonosulfate (PMS) for the rapid degradation of *p*-ASA while simultaneously immobilizing inorganic arsenic. CoPW was loaded into the nano layer of LDH through a simple ion exchange method, LDH-CoPW with a confined structure possessed independent adsorption and catalytic sites, the confined CoPW acted as the activator for PMS activation while the LDH layer was responsible for the adsorption of inorganic arsenic. Non-interfering operation of the active sites endowed LDH-CoPW with distinguished performance. Satisfactory removal of *p*-ASA and TOC by the LDH-CoPW/PMS system was attributed to the long-acting oxidation capacity of Co(IV)=O. By calculating the second-order reaction rate constants of Co(IV)=O with probes for the first time, we determined the striking contribution of Co(IV)=O to the *p*-ASA degradation via the probe-based kinetic model, and revealed the underlying mechanism of PMS activation. This work lies in providing a catalyst synthesis strategy that mitigates the antagonism between active sites and elucidating the activation mechanism of PMS by LDH-CoPW synthesized using this strategy.

Keywords: Confined catalysis; Polyoxometalates; Layered double hydroxides; High valence cobalt; *p*-arsanilic acid.

1. Introduction

Phenylarsenicals, including *p*-arsanilic acid (*p*-ASA) and roxarsone (ROX), have been extensively used as feed additives to promote the growth of livestock and control diseases in poultry since the 1970s [1]. However, phenylarsenicals are poorly metabolized by animals, and approximately 90% of phenylarsenicals are excreted into the environment in their raw form. This leads to contamination of source water through processes like biocomposting and surface runoff, posing significant ecological risks [2, 3]. Despite studies that have confirmed the low biotoxicity of phenylarsenicals, a critical aspect often overlooked is their potential decomposition and subsequent release of more toxic inorganic arsenic (As(III/V)) during microbial activities and sunlight irradiation [4, 5]. Therefore, it is imperative to implement measures for the proper disposal of phenylarsenicals to prevent the spread of associated risks.

Recently, peroxymonosulfate (PMS)-based advanced oxidation processes have attracted attention from researchers due to their satisfactory performance in the elimination of organic contaminants [6-8]. Despite achieving ultrafast degradation of phenylarsenicals using ferrous ions as PMS activators, the removal of inorganic arsenic still required the addition of a considerable dose of alkali to neutralize the solution pH and flocculate inorganic arsenic [2]. Hence, heterogeneous catalysts with both activation and adsorption functions are considered reliable substitutes for metal ion activators, capable of controlling the released inorganic arsenic in situ and alleviating the recovery difficulties of homogeneous catalysts. Chen et al. and Huang et al. reported on the PMS activation by $CuFe_2O_4$ for the removal of *p*-ASA and the simultaneous adsorption of inorganic arsenic. These studies showed that the use of catalysts

could greatly reduce the concentration of inorganic arsenic in the solution compared to the homogeneous catalytic system [1, 9].

Among the PMS activators, cobalt-containing catalysts have been considered to possess superior activity for boosting PMS activation. The removal of 50 μM of ROX by the Co_3O_4/PMS system reached nearly 50% within 2 min, demonstrating much higher efficiency compared to other metal-based catalysts [10]. However, while the combination of cobalt-based catalysts and PMS effectively decomposed phenylarsenicals, these catalytic systems were slightly insufficient in the adsorption of inorganic arsenic due to a lack of adsorption sites [3]. The continuous cumulative concentration of total inorganic arsenic in the solution treated by the Co_3O_4/PMS system reached 2.96 mg/L [10]. Therefore, it is urgent to propose optimization strategies for cobalt-based catalysts to enhance their effectiveness in remediating phenylarsenical-polluted water.

Layered double hydroxides (LDHs) are important clay materials commonly used as adsorbents for the removal of inorganic pollutants. Guo et al. synthesized Cu/Mg/Fe/La-LDH for the adsorption of arsenate in aqueous solution Through ion exchange and layer ligand exchange mechanisms, Cu/Mg/Fe/La-LDH exhibited a high adsorption capacity for arsenate, reaching 22.2 mg/g [11]. Some studies have evidenced that arsenate adsorption on magnesium-based LDHs was dominated by interlayer anion exchange while that over calcium-based LDHs occurred by means of precipitation of dissolved Ca^{2+} with arsenate [12]. These findings inspire us to leverage the spatial structure advantage of LDHs to assemble composite catalysts for achieving dual purposes. By confining the cobalt catalytic core within the LDH interlayer to

activate PMS for phenylarsenical degradation and utilizing calcium-based LDH as the adsorption core to enrich released inorganic arsenic, “two birds with one stone” can be realized.

In this study, $[Co_4(PW_9O_{34})_2]$ polyoxometalate cluster (CoPW) intercalated CaFe-LDH (LDH-CoPW) was prepared to activate PMS for the removal of *p*-ASA. CoPW nanocluster, as the main catalytic sites for the PMS activation, was confined in the interlayer of LDH nanosheet. The physicochemical properties and microstructure of LDH-CoPW were comprehensively characterized by a series of instruments. The performance of the LDH-CoPW/PMS system was tested under various conditions. Moreover, the conversion of arsenic species during the reaction and the arsenic accumulation by the catalyst were investigated. Finally, we revealed the underlying catalytic mechanism of the LDH-CoPW/PMS system and evaluated the toxicity inhibition potential of this system.

2. Materials and methods

2.1. Chemicals

Potassium peroxymonosulfate was acquired from Sigma-Aldrich®, and other reagents were purchased from Sinopharm Chemical Reagent Co., Ltd., China. All reagents were analytical grade and used as received without further purification. Ultrapure water was used in all experiments.

2.2. Synthesis of LDH-CoPW

The synthesis route of LDH-CoPW is shown in Fig. 1. CaFe-LDH was first prepared as the host of CoPW. Briefly, 20 mmol of $Ca(NO_3)_2{\cdot}4H_2O$ and 10 mmol of $Fe(NO_3)_3{\cdot}9H_2O$ were dissolved in 100 mL of ultrapure water to form salt solution. Then, the alkaline liquor was

prepared by dissolving 2.4 g of NaOH in another 100 mL of ultrapure water. Subsequently, the mixed metal salt solution was dropwise added to the NaOH solution with vigorous stirring under nitrogen atmosphere. Whereafter, the suspension was aged at 60 ℃ for 10 h to obtain CaFe-LDH. CoPW was synthesized according to the previous literature [13]. LDH-CoPW was synthesized with the method of ion exchange under nitrogen atmosphere. 0.5 g of CaFe-LDH was dispersed in 200 mL of ultrapure water. Then, 50 mL of ultrapure water containing 0.5 g of CoPW was added to the above suspension, the reaction was kept at 60 ℃ for 3 h. After filtration, washing and drying, the collected powder was named LDH-CoPW.

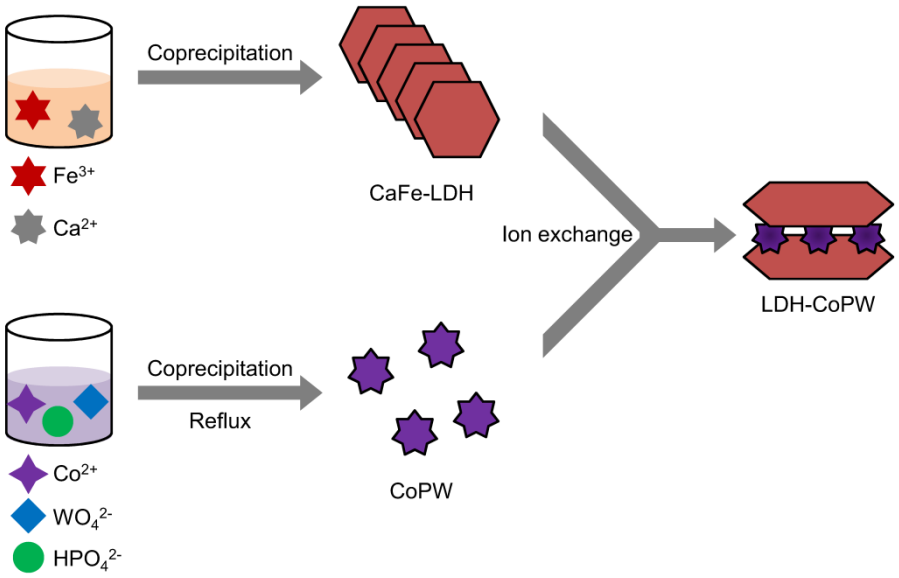

Figure 1. Schematic diagram of LDH-CoPW preparation.

Characterization, experimental, analytic and calculation methods are provided in Texts S1-S6 and Tab. S1 in Supporting Information.

3. Results and discussion

3.1. Catalysts characterization

The crystalline phase of LDH-CoPW was determined by XRD. As shown in Fig. 2a, peaks at 2θ = 6.8°, 18.7°, 28.8° and 46.5° corresponded to the (003), (006), (009) and (015) lattice planes of CaFe-LDH, respectively [14, 15]. Significantly, the splitting peaks around 2θ = 20° could be attributed to the impure calcium/iron carbonate, which is usually difficult to avoid in the synthesis of Ca and Fe based LDHs. Compared with the pristine CaFe-LDH, the replacement of NO_3^- by CoPW in the interlayer of CaFe-LDH resulted in a shift of lattice reflections to lower 2θ values, suggesting the successful intercalation of CoPW [16]. Specifically, the first basic reflection corresponding to the *d* value provided information about the interlayer distance [15]. As calculated, the basal spacing of LDH-CoPW (17.9 Å) was significantly higher than that of CaFe-LDH (8.2 Å). The interlayer spacing, calculated to be 13.1 Å by subtracting the height of the host layer (4.8 Å), was consistent with the diameter of the *b* axis of CoPW [13, 15].

HR-TEM was employed to observe the microstructure of LDH-CoPW. As can be seen in Fig. 2b, LDH-CoPW exhibited a typical lamellar structure of brucite and the standing-up nanosheets with a mean size of 50 nm were found in the bulk aggregates, suggesting the structure stability of CaFe-LDH during the ion exchange process. Moreover, the element content analysis and EDS-mapping of LDH-CoPW (Fig. 2c and d) verify that the as-prepared catalyst was consisted with uniformly distributed Ca, Fe, O, Co, P and W elements. Moreover, the molar ratio of Ca: Fe: Co: P: W in LDH-CoPW was determined to be 1: 1.9: 0.2: 0.1: 2.8 via ICP-OES with microwave digestion. Significantly, the relative content of Co belonging to

CoPW was much lower than that of Fe representing CaFe-LDH, demonstrating that compared to simple load, CoPW was more likely to be intercalated in the CaFe-LDH interlayer. Overall, the above results indeed verify the rational assembly of CaFe-LDH and CoPW.

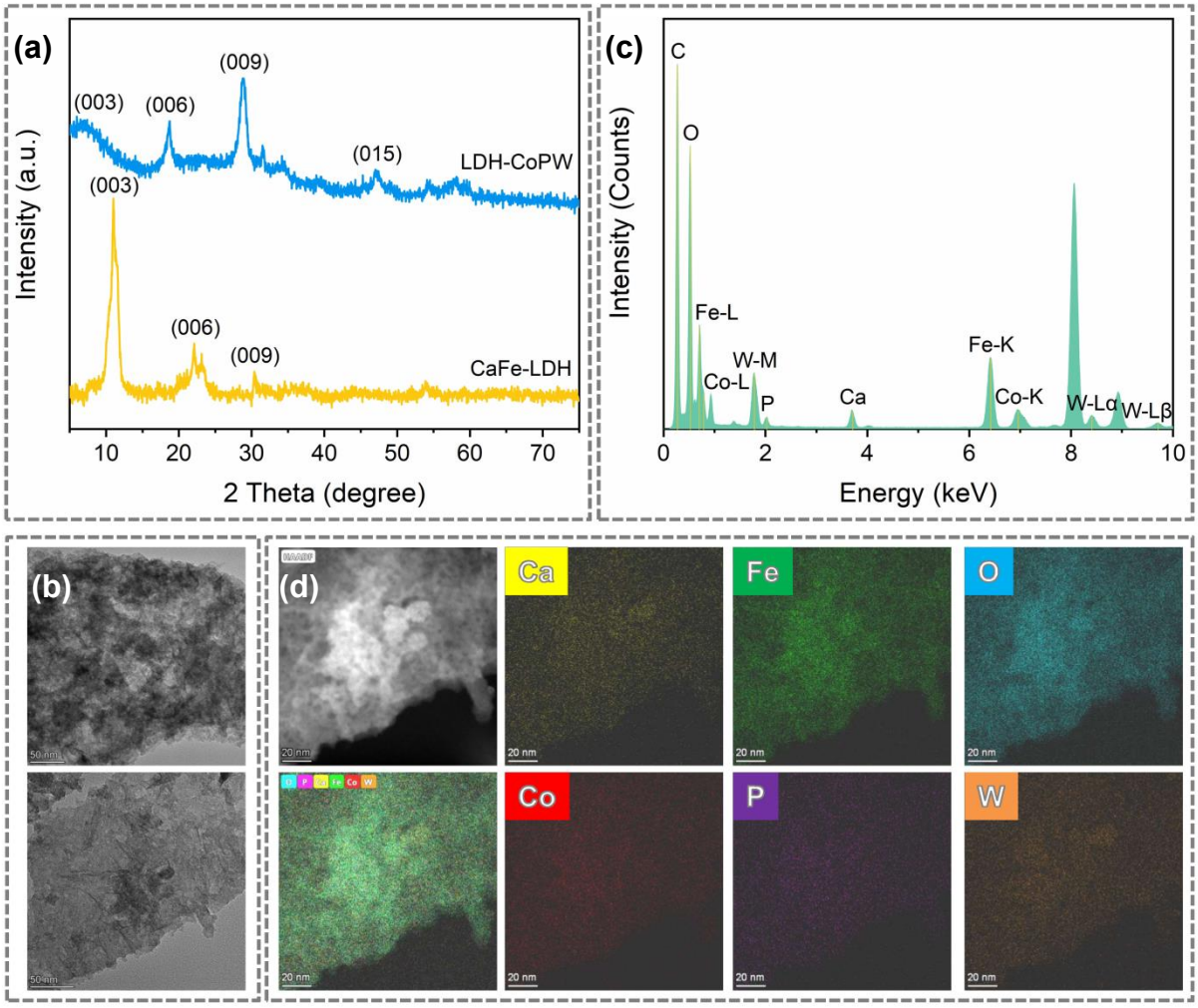

Figure 2. (a) XRD pattern of LDH-CoPW and CaFe-LDH; (b) HR-TEM, (c) element content analysis and (d) EDS-mapping of LDH-CoPW.

3.2. Catalytic performance evaluation

The performance of the LDH-CoPW/PMS system was assessed using *p*-ASA as the targeted pollutant. As displayed in Fig. 3a, the combination of LDH-CoPW and PMS

eliminated 93.8% of *p*-ASA within 20 min of reaction time. In contrast, the direct oxidation of PMS and the adsorption of LDH-CoPW resulted in only ~2% removal of *p*-ASA, implying the boosting of LDH-CoPW to the PMS activation. Moreover, the catalytic activity of CaFe-LDH and CoPW were tested as well. From ICP-OES analysis, the mass ratio of Co in LDH-CoPW was about 2%. Therefore, based on the molecular formula of CoPW, the CoPW dosage was considered as 0.05 g/L. As shown in Fig. 3b, the pseudo-first-order reaction rate constant (k_{obs}) for the LDH-CoPW/PMS, CoPW/PMS and CaFe-LDH/PMS systems were 0.09, 0.05 and 0.01 min^{-1}, respectively. This suggests that the main catalytic site of LDH-CoPW could be CoPW. Furthermore, the synergic coefficient (ξ) was used to determine the possible synergistic effect of CoPW and LDH ($\xi = k_{obs}$(LDH-CoPW/PMS)/[k_{obs}(CaFe-LDH/PMS) + k_{obs}(CoPW/PMS)]). As calculated, the ξ value was 1.5, definitely verifying the synergism between CoPW and LDH in LDH-CoPW. Furthermore, the turnover frequency values (TOF) of some reported catalysts were calculated by dividing the pseudo-first-order reaction rate constant by the product of catalyst dosage, PMS dosage, and *p*-ASA concentration. As calculated, the TOFs of $CuFe_2O_4$, pre-magnetized Fe^0 and Co_3O_4-La_2CO_5@RSBC were 0.015, 0.085 and 0.273, which were much lower than that of LDH-CoPW (0.9) (Tab. S2), suggesting the superior performance of LDH-CoPW [1, 17, 18].

To further estimate the mineralization ability of the LDH-CoPW/PMS system, the TOC removal during the reaction was monitored. As described in Fig, 3c, along with 93.8% of *p*-ASA being degraded, 57.4% of TOC was eliminated within 20 min of reaction time. This implies that a considerable concentration of *p*-ASA was still being degraded into other

intermediates with potential toxicity. Interestingly, with the reaction time prolonged to 60 min, the mineralization rate further improved to 86.1%, suggesting the generation of reactive species with long-acting oxidation capacity in the LDH-CoPW/PMS system. Furthermore, the concentrations of Ca, Fe, Co, P and W ions leaked from the catalyst during the reaction were only 31.5, 41.4, 22.6, 8.2 and 114.2 μg/L, respectively, suggesting the environmental friendliness of the LDH-CoPW/PMS system. The effect of reaction temperature on the *p*-ASA degradation was investigated as shown in Fig. 3d, higher temperatures promoted the PMS activation by LDH-CoPW, as k_{obs} for the *p*-ASA degradation at 15 ℃, 25 ℃, 35 ℃ and 45 ℃ were 0.06, 0.09, 0.25 and 0.40 min^{-1}, respectively. The inserted figure in Fig. 3d reveals a linear relationship between $\ln(k_{obs})$ and the reciprocal of the reaction temperature (1/T), with the activation energy (Ea) of PMS by LDH-CoPW calculated to be 49.0 kJ/mol. Considering that the Ea of diffusion-controlled reactions typically falls within the range of 10-13 kJ/mol, it suggests that the catalytic reaction is controlled by surface chemical reactions rather than mass transfer [19].

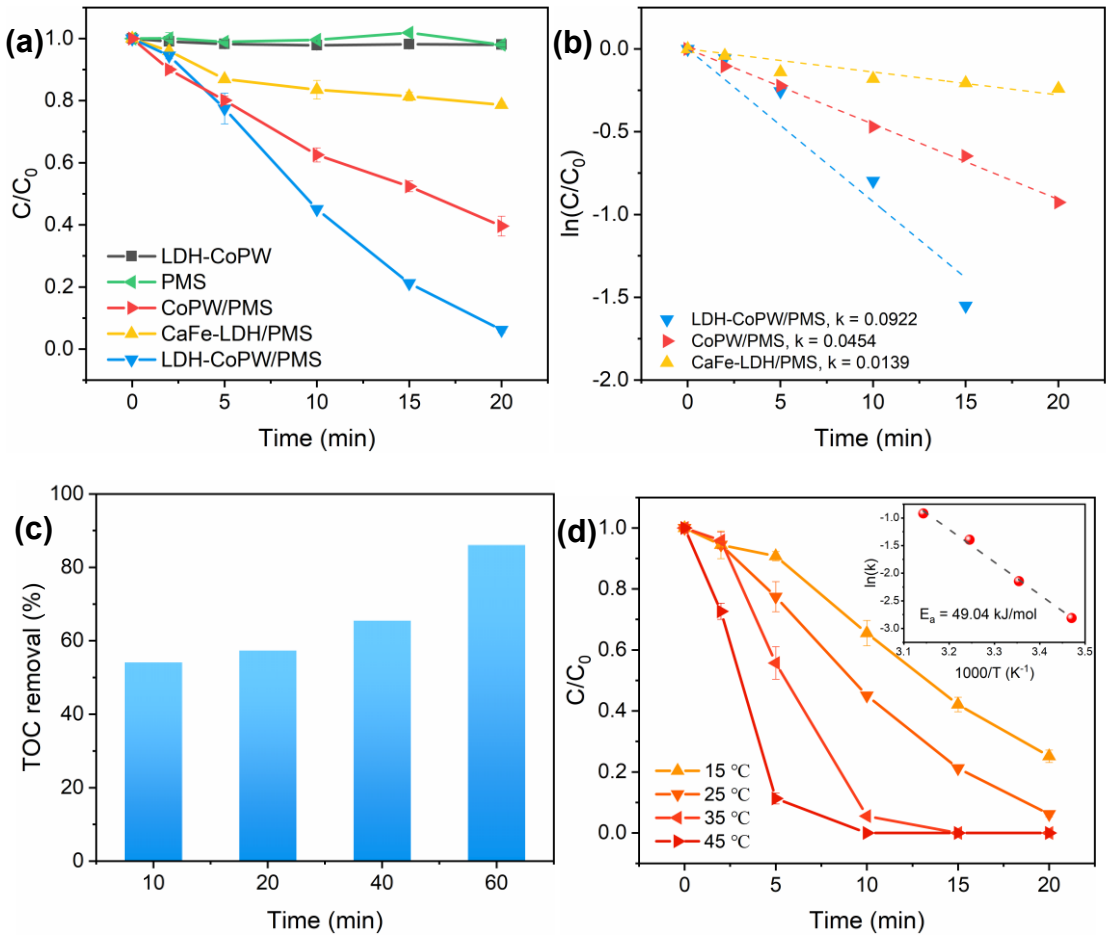

Figure 3. (a) *p*-ASA degradation and (b) correlation coefficient of *p*-ASA degradation in different catalytic systems; (c) TOC removal in LDH-CoPW/PMS system; (d) Effect of temperature on *p*-ASA degradation in LDH-CoPW/PMS system ([Catalyst] = 0.1 g/L, [PMS] = 0.1 mM, [*p*-ASA] = 10 mg/L).

3.3. Arsenic immobilization

Considering the deadlier toxicity of inorganic arsenic than *p*-ASA, the release of inorganic arsenic and the transformation of arsenic species during the *p*-ASA attenuation were monitored. As displayed in Fig. S1, The *p*-ASA degradation induced by the LDH-CoPW/PMS system caused a remarkable increase in the accumulation of inorganic arsenic in the solution, reaching peak concentrations of total As, As(III) and As(V) of 2.02, 0.45 and 1.57 mg/L, respectively,

within 15 min. With the reaction time prolonged to 180 min, the concentrations of total As and As(V) gradually declined to 1.60 and 1.15 mg/L, while the concentration of As(III) basically stabilized at 0.45 mg/L. This might be related to the higher K_{sp} of As(III) compared to As(V), and $Ca_3(AsO_4)_2$ formed by the reaction of As(V) and Ca(II) was the main component of the catalyst surface precipitation [20, 21]. Therefore, a dynamic equilibrium between As(III) released from *p*-ASA and oxidized As(III) was achieved. Finally, according to the mass balance of As species, 53.6% of inorganic arsenic was adsorbed by LDH-CoPW, suggesting the reliable performance of the LDH-CoPW/PMS system in *p*-ASA removal. The residual inorganic arsenic in the solution treated by the catalytic system still exceeded the environmental standard. However, it is worth noting that for the convenience of kinetic studies, the concentration of *p*-ASA in this study was also far higher than that in natural water environment. When the catalytic system is applied in the actual water treatment, the adsorption capacity of LDH-CoPW (18.5 mg/g) for As is sufficient to ensure the safe concentration of inorganic arsenic in water. Despite the surface functional groups and crystal structure of LDH-CoPW barely changing after the reaction (Fig. S2a and b), it is still reasonable to believe that As(V) was indeed adsorbed on the catalyst surface. This is because As(V) was mainly removed by forming $Ca_3(AsO_4)_2$, which would not lead to new infrared absorption peaks, meanwhile, the determination of amorphous or low content of $Ca_3(AsO_4)_2$ by XRD was ineffective. Herein, the XPS As 3d spectrum of the used LDH-CoPW (Fig. S3) undoubtedly verifies the adsorption of As(V) on the LDH-CoPW surface, with the peak at a binding energy of 45.5 eV usually considered to be related to As(V) [10].

3.4. Catalytic mechanisms analysis

3.4.1. Reactive species identification

Reactive species (RSs), including radicals, singlet oxygen ($^1O_2$) and high valence cobalt (Co(IV)=O), could be produced in the catalytic system during PMS activation [22, 23]. Therefore, it is necessary to first determine the RSs existing in the LDH-CoPW/PMS system. ESR analysis was employed to distinguish sulfate radical ($SO_4^{\bullet-}$), hydroxyl radical ($^{\bullet}OH$), superoxide radical ($O_2^{\bullet-}$) and $^1O_2$ using 5,5-dimethyl-1-pyrroline N-oxide (DMPO) and 2,2,6,6-Tetramethylpiperidine (TEMP) as the trapping agents. From Fig. 4a, instead of the signal of DMPO-$SO_4^{\bullet-}$ and DMPO-$^{\bullet}OH$ adducts, a seven-line characteristic signal related to 5,5-dimethyl-1-pyrrolidone-2-oxy-l (DMPOX) adducts was found in the LDH-CoPW/PMS system. Although DMPOX was once considered to be the excessive oxidation of DMPO by radicals, some studies have also suggested that Co(IV)=O can directly oxidize DMPO to produce DMPOX, leading to potentially misleading information [24]. Thus, methyl phenyl sulfoxide (PMSO), which can be selectively oxidized by Co(IV)=O to produce methyl phenyl sulfone ($PMSO_2$), was applied to identify Co(IV)=O in the system [25]. As shown in Fig. 4b, compared with the sole PMS system, the introduction of LDH-CoPW tremendously accelerated the PMSO degradation and $PMSO_2$ formation, reliably indicating the generation of Co(IV)=O in the LDH-CoPW/PMS system. Furthermore, the six-line and three-line characteristic signals (Fig. 4c) can be attributed to DMPO-$O_2^{\bullet-}$ and TEMP-$^1O_2$ adducts, indicating the formation of $O_2^{\bullet-}$ and $^1O_2$ in the LDH-CoPW/PMS system [26].

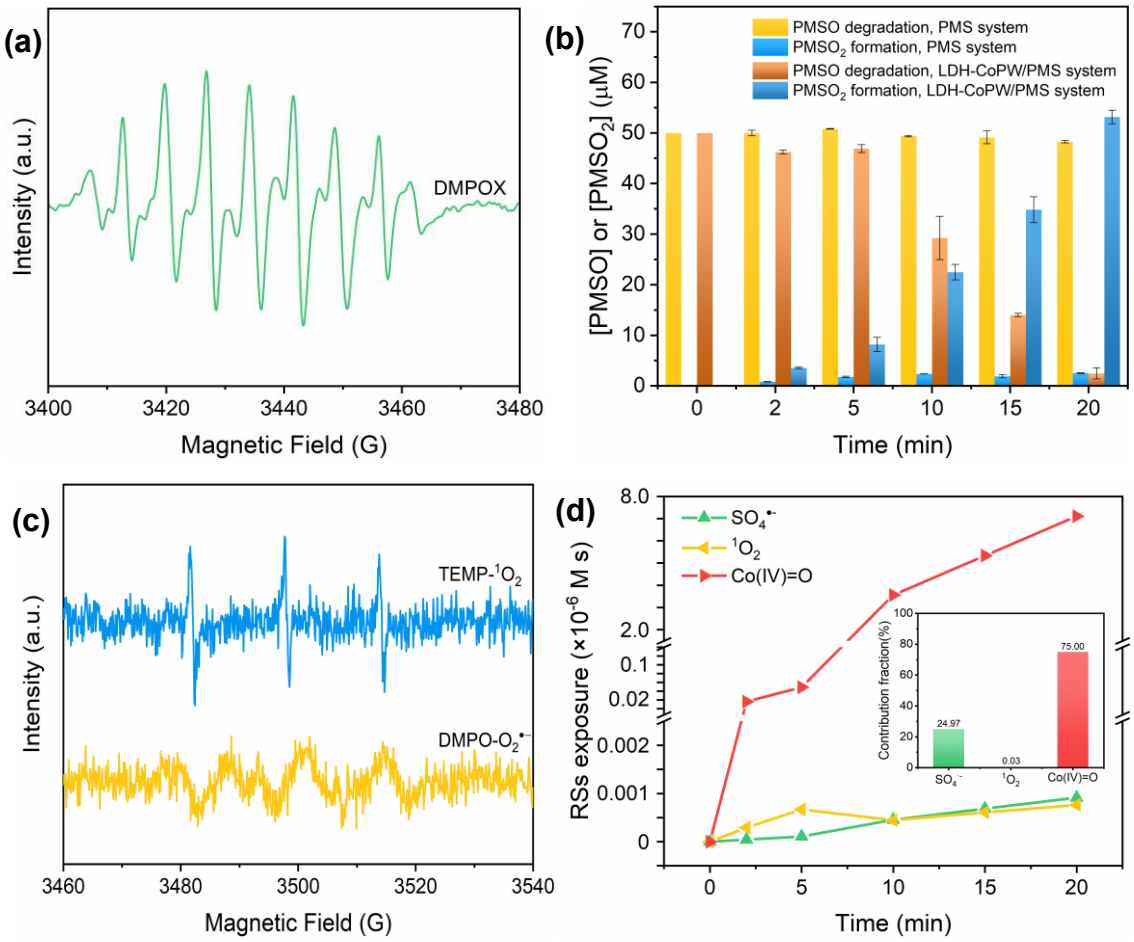

Figure 4. (a) ESR spectra of DMPO-$SO_4^{\bullet-}$ and DMPO-$^{\bullet}OH$; (b) $PMSO_2$ production using PMSO as probe in LDH-CoPW/PMS system; (c) ESR spectra of DMPO-$O_2^{\bullet-}$ and TEMP-$^1O_2$; (d) RS exposure and contribution fraction to *p*-ASA degradation ([Catalyst] = 0.1 g/L, [PMS] = 0.1 mM, [*p*-ASA] = 10 mg/L).

Recently, electron transfer process (ETP) has been regarded as one of the widely existing nonradical pathway for the degradation of organic pollutants. Therefore, a premixing experiment was carried out to discern the possible ETP [27]. From Fig. S4, the *p*-ASA degradation was greatly promoted when premixing LDH-CoPW and PMS for 5 min. This experimental phenomenon is intriguing, if the *p*-ASA degradation was dominated by ETP, the premixing of catalyst and PMS would have a small effect on the *p*-ASA oxidation. However,

if the process was dominated by radicals, the *p*-ASA degradation would be inhibited due to the consumption of radicals with a short half-life [28, 29]. A credible explanation for this is that Co(IV)=O with long-acting oxidation capacity might be generated in the LDH-CoPW/PMS system [30, 31]. Significantly, as the premixing time was prolonged to 15 min, the boosting of the catalytic reaction by premixing weakened, indicating the deactivation of Co(IV)=O.

3.4.2. Reactive species exposure

The above results indicate that there were at least three RSs: Co(IV)=O, $O_2^{\bullet-}$ and $^1O_2$, in the LDH-CoPW/PMS system. For $O_2^{\bullet-}$ with a negative redox potential (-0.8 V), the direct oxidation of *p*-ASA by $O_2^{\bullet-}$ was insignificant [32]. Hence, the roles of $SO_4^{\bullet-}$, $^{\bullet}OH$, $^1O_2$ and Co(IV)=O in the *p*-ASA degradation were evaluated. In this study, to avoid misleading conclusions from traditional quenching experiments, the probe-based kinetic model proposed by Wang's group was performed to evaluate the RSs exposure and contribution to the *p*-ASA degradation (details in Text S4) [33]. As shown in Fig. S5c, atrazine (ATZ), primidone (PMD), metronidazole (MTZ) and PMSO were used as probes for $SO_4^{\bullet-}$, $^{\bullet}OH$, $^1O_2$ and Co(IV)=O, respectively [34]. It is evident that all four probes were rapidly degraded by the LDH-CoPW/PMS system, confirming the presence of the four RSs in the solution. It is important to note that except for ATZ, two oxidation stages were observed in the PMD, MTZ and PMSO degradation processes (Fig. S5c). Thus, piecewise kinetic fitting was performed to accurately determine RSs exposure. As displayed in Fig. S5d, k_{obs} for the ATZ, PMD, MTZ and PMSO degradation were 0.08, 0.02/0.09, 0.02/0.22 and 0.04/0.54 min^{-1}, respectively. By calculation, the $^{\bullet}OH$ exposure was almost undetectable, while the exposures of $SO_4^{\bullet-}$, $^1O_2$ and Co(IV)=O

elevated continuously during the catalytic reaction, reaching 9.14×10^{-10}, 7.63×10^{-10} and 7.11×10^{-6} M s at 20 min, respectively (Fig. 4d). Furthermore, the variation of RSs transient concentration during the reaction was also estimated (details in Text S5). As shown in Fig. S6b, the $SO_4^{\bullet-}$, $^1O_2$ and Co(IV)=O concentrations increased slowly to 2.8×10^{-15}, 2.0×10^{-14} and 1.2×10^{-12} M within 2 min. However, their transient concentration variations diverged after 2 min of reaction time. Of which, the $^1O_2$ concentration continually declined to 5.3×10^{-15} M, while that of $SO_4^{\bullet-}$ and Co(IV)=O decreased slightly at first and then elevated significantly to 6.9×10^{-15} and 5.4×10^{-11} M. Then, the deficiency of PMS led to a slow decline in the $SO_4^{\bullet-}$ and Co(IV)=O concentration at the later stage of the reaction. Strikingly, the Co(IV)=O concentration was about 10^2-10^4 times higher than that of $SO_4^{\bullet-}$ and $^1O_2$ throughout the reaction, suggesting the dominant role of Co(IV)=O in the LDH-CoPW/PMS system. Based on the above, the contribution of different RSs to the *p*-ASA degradation was calculated as described in the inserted figure in Fig. 4d (details in Text S5). Although $^1O_2$ with the same concentration as $SO_4^{\bullet-}$ was yielded in the LDH-CoPW/PMS system, its contribution to the *p*-ASA attenuation was negligible. Meanwhile, the contribution of Co(IV)=O with long-acting oxidation capacity to the *p*-ASA degradation was as high as 75.0%, whereas the contribution of $SO_4^{\bullet-}$, despite its higher reactivity, was only 25.0% due to its lower concentration and shorter half-life compared to Co(IV)=O [30, 31].

3.4.3. Mechanism of PMS activation

Different from traditional PMS-based advanced oxidation processes, nonradical Co(IV)=O was identified as the dominant RSs in the LDH-CoPW/PMS system. Additionally,

the piecewise generation of $SO_4^{\bullet-}$ and Co(IV)=O also left us with confusion. We speculate that the unique PMS activation mechanism might be related to the special confined structure of LDH-CoPW. The element valence of LDH-CoPW before and after the catalytic reaction was determined using XPS. As shown in Fig. 5, the 2p orbit can be divided into $2p_{1/2}$ and $2p_{3/2}$, representing the same elemental information. Herein, taking $2p_{3/2}$ as an example, the peaks at the binding energies of 780.8 and 784.9 eV were indexed to Co(III) and Co(II) (Fig. 5a), while Fe(III) and Fe(II) can be reflected by signals at the binding energies of 712.2 and 710.0 eV, respectively (Fig. 5b) [35, 36]. From Tab. S4, obviously, the relative content of Co(III) reduced from 62.7% to 59.4%, denying the single-electron PMS activation that commonly accompanies the conversion of Co(II) to Co(III) (Eq. 1) [37]. This result further verifies that Co(IV)=O was formed through two-electron transfer from Co(II) to PMS, which led to the generation of SO_4^{2-} (Eq. 2) [38]. As for Fe species, 0.6% of Fe(II) was oxidized to Fe(III) after the reaction, suggesting the participation of Fe species in the redox cycle of Co species (Eq. 3) [39]. Besides, the PMS activation by Fe(II) to produce $SO_4^{\bullet-}$ could also result in the increase of Fe(III) (Eq. 4) [40]. According to the XPS analysis, it can be confirmed that the intercalated CoPW in the confined space of CaFe-LDH was the cause of the formation of Co(IV)=O. Due to the buffering of CaFe-LDH, the coordination of CoPW and PMS via inner/outer sphere interaction would not be interfered with by ClO_4^- and PO_4^{3-} (Fig. S7) [19]. Meanwhile, CaFe-LDH was responsible for accelerating the redox cycle of Co species and activating PMS to produce $SO_4^{\bullet-}$. For the generation of $^1O_2$, the presence of $O_2^{\bullet-}$ confirmed by ESR analysis reveals the possibility of the transformation from $O_2^{\bullet-}$ to $^1O_2$ (Eq. 5) [23]. Moreover, the self-

decomposition of PMS was also considered to be one of the pathways to produce $^1O_2$ (Eq. 6) [41].

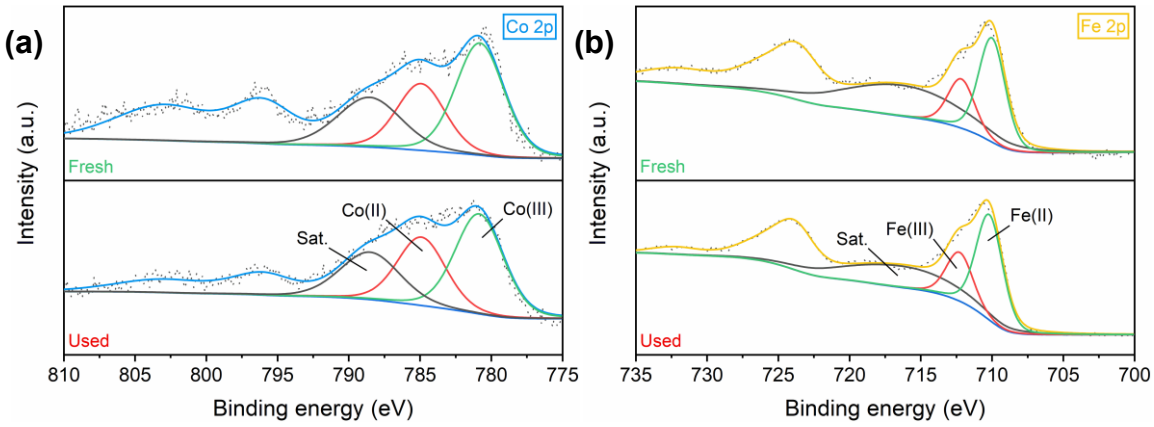

Figure 5. XPS spectra of fresh and used LDH-CoPW: (a) Co 2p and (b) Fe 2p.

$$Co(II) + HSO_5^- \rightarrow Co(III) + SO_4^{\bullet-} + OH^- \quad (1)$$

$$Co(II) + HSO_5^- \rightarrow Co(IV)=O + SO_4^{2-} + H^+ \quad (2)$$

$$Co(III) + Fe(II) \rightarrow Co(II) + Fe(III) \quad (3)$$

$$Fe(II) + HSO_5^- \rightarrow Fe(III) + SO_4^{\bullet-} + OH^- \quad (4)$$

$$O_2^{\bullet-} + H_2O \rightarrow {}^1O_2 + H_2O_2 + OH^- \quad (5)$$

$$HSO_5^- + SO_5^{2-} \rightarrow 2SO_4^{2-} + {}^1O_2 + H^+ \quad (6)$$

Given the above, the mechanism of the *p*-ASA removal by the LDH-CoPW/PMS system is proposed as described in Fig. 6, under the buffering of CaFe-LDH, PMS added to the solution could not be activated immediately. With the mass transfer of PMS to the interlayer of CaFe-LDH, the hydroxyl group of CoPW would be substituted by HSO_5^- to form CoPW-$OOSO_3^-$ intermediate. Then, oxygen atom transfer occurred between CoPW and PMS via two electron-

transfer from Co(II) to $OOSO_3^-$, accompanied by the production of Co(IV)=O. Although Co(IV)=O would only be reduced to Co(III) during the *p*-ASA degradation, the Fe sites on the CaFe-LDH layer could boost the reduction of Co(III) to Co(II), further ensuring the sustainability of the reaction. Simultaneously, the inorganic arsenic released during the *p*-ASA degradation existed predominantly as As(V) in the highly oxidizing environment and can be immobilized in situ by CaFe-LDH, thereby reducing the risk of arsenic contamination.

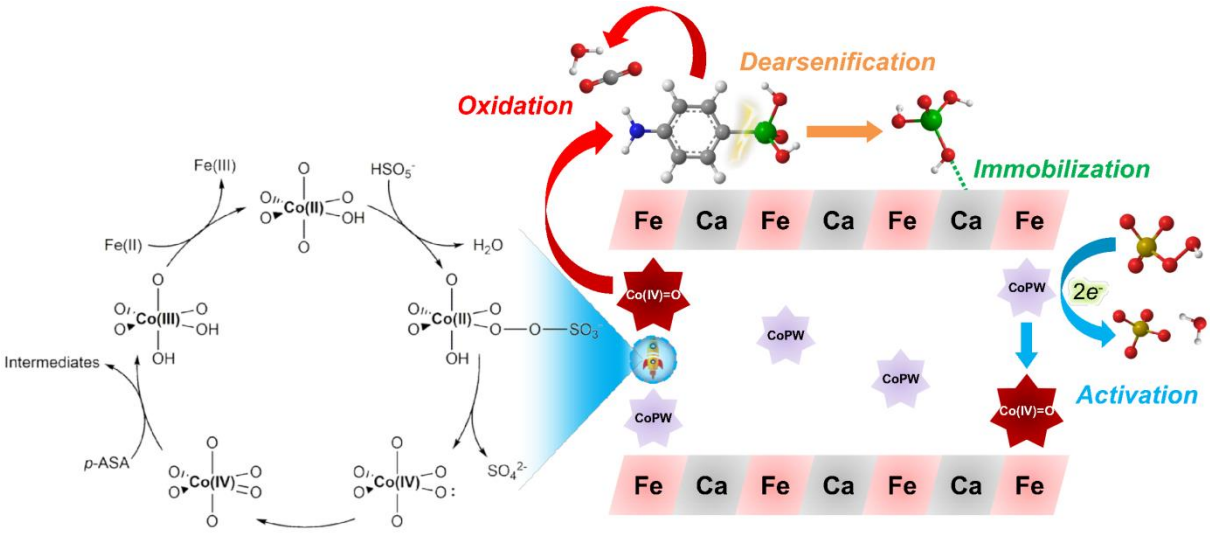

Figure 6. Proposed mechanism of *p*-ASA removal by LDH-CoPW/PMS system.

3.5. Effect of key parameters

As shown in Fig. S8a, the LDH-CoPW/PMS system possessed satisfactory performance in neutral, mildly acidic and alkaline solutions, with k_{obs} for the *p*-ASA degradation at pH 5.0, 7.0 and 9.0 being 0.09, 0.12 and 0.12 min^{-1}, respectively. However, the catalytic efficiency of the LDH-CoPW/PMS system was remarkably suppressed at pH 3.0, and only 30.2% of *p*-ASA was removed within 20 min. Due to the acidity of PMS, the pH values variation during the

reaction at different initial pH was monitored as shown in Fig. S9a, the appearance of PMS resulted in a change of solution pH from 3.0, 5.0, 7.0, and 9.0 to 3.5, 4.4, 4.8, and 5.7, respectively. As shown in Fig. S9b, HSO_5^- was the main existing species in the studied pH range, while *p*-ASA gradually transformed from zwitterion to anions with the increase of pH value. Meanwhile, attributed to the abundant hydroxyl groups on the LDH-CoPW surface, the catalyst was always negatively charged. In this case, the electrostatic repulsion between the catalyst, *p*-ASA and PMS elevated gradually with increasing solution pH, which could inhibit the reaction. However, no significant reduction in performance was observed in this study. A credible explanation is that the confined space of LDH buffered the change in the surface chemistry micro-environment of the intercalated CoPW [42]. Moreover, the structural collapse of CaFe-LDH under overly acidic condition might be responsible for the deterioration of the catalyst [43].

The effect of coexisting anion on the LDH-CoPW/PMS system was evaluated. From Fig. S8b, the participation of Cl^- evidently suppressed the *p*-ASA degradation, more specifically, the higher dosage of Cl^- could lead to more serious inhibition, with k_{obs} for the *p*-ASA degradation declining to 0.04 min^{-1} with the increase of Cl^- concentration to 10 mM. This might be due to the direct consumption of PMS by excessive Cl^- [44]. The addition of SO_4^{2-} slightly deteriorated the catalytic efficiency of the LDH-CoPW/PMS system, with k_{obs} for the *p*-ASA degradation being 0.08, 0.07 and 0.06 min^{-1} in the presence of 1, 5 and 10 mM of SO_4^{2-}, respectively (Fig. S8c). Generally, SO_4^{2-} can reduce the redox potential of HSO_5^-/SO_4^{2-}, thereby suppressing the formation of Co(IV)=O [45]. Furthermore, NO_3^- barely affected the

reactivity of the LDH-CoPW/PMS system. Overall, the effect of coexisting anions on the catalytic system performance was limited, indicating promising application prospects for the LDH-CoPW/PMS system.

3.6. Degradation intermediates and ecotoxicity analysis

Insufficient mineralization of *p*-ASA implies the accumulation of degradation intermediates in the solution. Thus, HPLC-MS was carried out to identify the intermediates with potential toxicity. As shown in Fig. S10, nine organic compounds, including *p*-ASA, were found in the solution by analyzing the mass-to-charge values. Meanwhile, DFT calculation was used to further explicate the degradation pathways of *p*-ASA. Fig. S11 shows that 11N atom with the highest f^- value was sensitive to the attack of Co(IV)=O and easily oxidized. Besides, 11N atom also possessed the highest f^0 value, suggesting that 11N atom was vulnerable to be attacked by RSs via hydroxylation. Significantly, 1As and 5C atoms also possessed relatively high f^0 values, indicating that *p*-ASA was prone to releasing inorganic arsenic through dearsenification. Therefore, the *p*-ASA degradation routes were proposed as illustrated in Fig. 7a, the As-C bond on the benzene ring was initially attacked by RSs, leading to the release of As species and the formation of P1. For the inorganic part, the released arsenic could be immobilized on the LDH surface in situ. Regarding the organic part, on the one hand, highly reactive Co(IV)=O could oxidize P1 to form P2 via oxygen atom transfer, and P3 was further obtained through the hydroxylation of P2 [9]. On the other hand, P4 and P5 can be generated via the progressive hydroxylation of P1, of which, P5 would rapidly transform to P6 in the oxidizing environment [46]. Due to the polymerization-induced property of Co(IV)=O, P1 and

P3 can polymerize to form P8 under the attack of Co(IV)=O, and P7 could be produced via the self-polymerization of P4 [47].

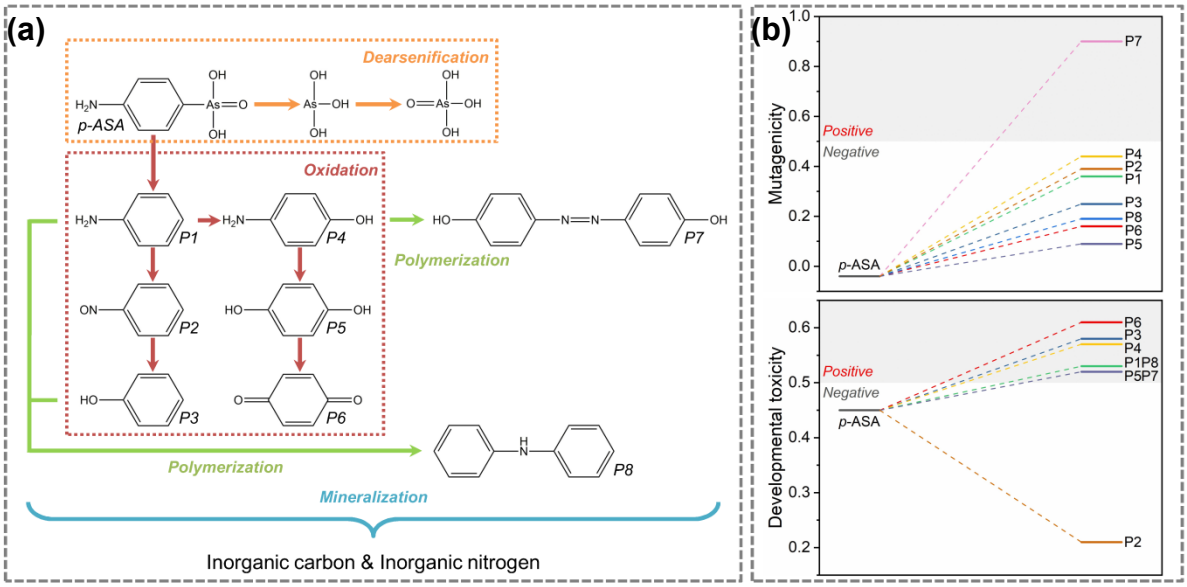

Figure 7. (a) Degradation pathway of *p*-ASA; (b) Toxicity evaluation of degradation intermediates by T.E.S.T. program.

The ecotoxicity of *p*-ASA and its degradation intermediates was further evaluated using T.E.S.T. program developed by the Environmental Protection Agency. As displayed in Fig. 7b, *p*-ASA possessed negative mutagenicity, while the mutagenicity of all intermediate products improved during the process, luckily, except for P7, the other products still exhibited negative mutagenicity, suggesting the routine attention to P7 and its polymeric monomer P4 was necessary. As for the developmental toxicity, the situation was less optimistic, *p*-ASA with negative developmental toxicity was degraded to seven products with positive developmental toxicity, and only the developmental toxicity of P2 was obviously suppressed. This highlights the importance of achieving higher mineralization rather than simply diluting *p*-ASA.

Significantly, the LDH-CoPW/PMS system with Co(IV)=O as the main RSs possessed longer-acting oxidation capacity, which would be beneficial to the suppression of toxicity.

4. Conclusion

A promising strategy for mitigating arsenic pollution using LDH-CoPW boosted PMS activation was proposed in this work. 93.8% of *p*-ASA and 57.4% of TOC can be attenuated by the LDH-CoPW/PMS system within 20 min. The nano confined structure of LDH-CoPW allows CoPW and LDH to operate independently as the catalytic and adsorption sites, respectively. Thus, the inorganic arsenic released with the rapid degradation of *p*-ASA can be directly immobilized on the surface of LDH-CoPW through the adsorption site. From the mechanism study, the participation of radical and nonradical involved in the *p*-ASA degradation were determined using probe experiments and ESR analysis. Despite some initially confusing experimental results, we unequivocally verified the significant contribution of Co(IV)=O to the *p*-ASA degradation by the probe-based kinetic model. Toxicity analysis showed that the vast majority of degradation intermediates exhibited higher toxicity than *p*-ASA, fortunately, the LDH-CoPW/PMS system possessed excellent mineralization performance and could prevent the accumulation of toxic components.

Conflicts of interest

The authors declare no conflict of interest.

Supporting Information

XRD pattern, variation of arsenic species, FTIR and XRD pattern, As 3d XPS spectra, premixing experiments, probe-based kinetic experiments, effect of water matrix, mass

spectrum, DFT calculation

Acknowledgments

This work was supported by National Natural Science Foundation of China (Grant No. 52300014 and 51978618), Zhejiang Provincial Natural Science Foundation of China (Grant No. LQ24E080020 and LZ24E080005). The authors would like to thank Shiyanjia Lab (www.shiyanjia.com) for the XPS analysis.

References

[1] Chen, S., Deng, J., Ye, C., Xu, C., Huai, L., Li, J., Li, X. Simultaneous removal of para-arsanilic acid and the released inorganic arsenic species by $CuFe_2O_4$ activated peroxymonosulfate process. *Sci. Total Environ.* **2020**, 742, 140587.

[2] Cai, A., Ling, X., Wang, L., Sun, Q., Zhou, S., Chu, W., Li, X., Deng, J. Insight into UV-LED/PS/Fe(III) and UV-LED/PMS/Fe(III) for p-arsanilic acid degradation and simultaneous arsenate immobilization. *Water Res.* **2022**, 223, 118989.

[3] Liu, L., Jing, Z., Zhang, M., Zhao, X., Lan, Y., Chen, C. Fabrication of magnetic bifunctional composite via anchoring CoY on waste heating pad as a cycling material for peroxymonosulfate activation to degrade p-arsanilic acid and simultaneously eliminate secondary As(V). *Chem. Eng. J.* **2023**, 459, 141641.

[4] Yang, T., An, L., Zeng, G., Jiang, M., Li, J., Liu, C., Jia, J., Ma, J. Efficient removal of p-arsanilic acid and arsenite by Fe (II)/peracetic acid (Fe (II)/PAA) and PAA processes. *Water Res.* **2023**, 241, 120091.

[5] Ye, C., Deng, J., Huai, L., Cai, A., Ling, X., Guo, H., Wang, Q., Li, X. Multifunctional capacity of CoMnFe-LDH/LDO activated peroxymonosulfate for p-arsanilic acid removal and inorganic arsenic immobilization: Performance and surface-bound radical mechanism. *Sci. Total Environ.* **2022**, 806, 150379.

[6] Yin, K., Peng, L., Chen, D., Liu, S., Zhang, Y., Gao, B., Fu, K., Shang, Y., Xu, X. High-loading of well dispersed single-atom catalysts derived from Fe-rich marine algae for boosting Fenton-like reaction: Role identification of iron center and catalytic mechanisms. *Appl. Catal. B-Environ.* **2023**, 336, 122951.

[7] Yin, K., Wu, R., Shang, Y., Chen, D., Wu, Z., Wang, X., Gao, B., Xu, X. Microenvironment modulation of cobalt single-atom catalysts for boosting both radical oxidation and electron-transfer process in Fenton-like system. *Appl. Catal. B-Environ.* **2023**, 329, 122558.

[8] Zeng, H., Zhu, H., Deng, J., Shi, Z., Zhang, H., Li, X., Deng, L. New insight into peroxymonosulfate activation by CoAl-LDH derived CoOOH: Oxygen vacancies rather than Co species redox pairs induced process. *Chem. Eng. J.* **2022**, 442, 136251.

[9] Huang, Y., Li, X., Zhang, C., Dai, M., Zhang, Z., Xi, Y., Quan, B., Lu, S., Liu, Y. Degrading arsanilic acid and adsorbing the released inorganic arsenic simultaneously in aqueous media with $CuFe_2O_4$ activating peroxymonosulfate system: Factors, performance, and mechanism. *Chem. Eng. J.* **2021**, 424, 128537.

[10] Chen, C., Liu, L., Li, Y., Zhou, L., Lan, Y. Efficient degradation of roxarsone and simultaneous in-situ adsorption of secondary inorganic arsenic by a combination of Co_3O_4-Y_2O_3 and peroxymonosulfate. *J. Hazard. Mater.* **2021**, 407, 124559.

[11] Guo, Y., Zhu, Z., Qiu, Y., Zhao, J. Adsorption of arsenate on Cu/Mg/Fe/La layered double hydroxide from aqueous solutions. *J. Hazard. Mater.* **2012**, 239-240, 279-288.

[12] Xu, Y., Dai, Y., Zhou, J., Xu, Z.P., Qian, G., Lu, G.Q.M. Removal efficiency of arsenate and phosphate from aqueous solution using layered double hydroxide materials: intercalation vs. precipitation. *J. Mater. Chem.* **2010**, 20, 4684-4691.

[13] Yin, Q., Tan, J.M., Besson, C., Geletii, Y.V., Musaev, D.G., Kuznetsov, A.E., Luo, Z., Hardcastle, K.I., Hill, C.L. A fast soluble carbon-free molecular water oxidation catalyst based on abundant metals. *Science.* **2010**, 328, 342-345.

[14] Szabados, M., Kónya, Z., Kukovecz, Á., Sipos, P., Pálinkó, I. Structural reconstruction of mechanochemically disordered CaFe-layered double hydroxide. *Appl. Clay Sci.* **2019**, 174, 138-145.

[15] Terzi, C.M., dos Santos, E.H., Carvalho, C., Prevot, V., Wypych, F., Forano, C., Nakagaki, S. MgAl and ZnAl layered double hydroxides modified with molybdate and tungstate anions as catalysts for oxidation of cyclohexane. *Catal. Today.* **2023**, 422, 114221.

[16] Sadavar, S.V., Padalkar, N.S., Shinde, R.B., Patil, A.S., Patil, U.M., Magdum, V.V., Chitare, Y.M., Kulkarni, S.P., Kale, S.B., Bulakhe, R.N., Bhange, D.S., Kochuveedu, S.T., Gunjakar, J.L. Lattice engineering exfoliation-restacking route for 2D layered double hydroxide hybridized with 0D polyoxotungstate anions: Cathode for hybrid asymmetric supercapacitors. *Energy Storage Mater.* **2022**, 48, 101-113.

[17] Chen, S., Deng, J., Ye, C., Xu, C., Huai, L., Ling, X., Li, J., Li, X. Degradation of p-arsanilic acid by pre-magnetized Fe^0/persulfate system: Kinetics, mechanism, degradation pathways and DBPs formation during subsequent chlorination. *Chem. Eng. J.* **2021**, 410, 128435.

[18] Li, Y., Liu, L., Wang, Z., Zhou, L., Lan, Y., Chen, C. Simultaneous oxidation of 4-aminophenylarsonic acid and adsorption of the produced inorganic arsenic by a combination of Co_3O_4-La_2CO_5@RSBC with peroxymonosulfate. *Chem. Eng. J.* **2021**, 413, 127417.

[19] Zeng, H., Zhu, H., Deng, J., Liu, B., Zhou, S., Shi, Z., Deng, L. Tunable peroxymonosulfate activation by (−111) crystal plane exposed δ-MnO_2: Oxidant concentration induced intrinsic mechanisms transformation. *Chem. Eng. J.* **2023**, 473, 145222.

[20] Zhu, Y.N., Zhang, X.H., Xie, Q.L., Wang, D.Q., Cheng, G.W. Solubility and stability of calcium arsenates at 25 °C. *Water, Air, Soil Pollut.* **2006**, 169, 221-238.

[21] Prasad, K.S., Ramanathan, A.L., Paul, J., Subramanian, V., Prasad, R. Biosorption of arsenite (As^{+3}) and arsenate (As^{+5}) from aqueous solution by Arthrobacter sp. biomass. *Environ. Technol.* **2013**, 34, 2701-2708.

[22] Zeng, H., Deng, L., Zhang, H., Zhou, C., Shi, Z. Development of oxygen vacancies

enriched CoAl hydroxide@hydroxysulfide hollow flowers for peroxymonosulfate activation: A highly efficient singlet oxygen-dominated oxidation process for sulfamethoxazole degradation. *J. Hazard. Mater.* **2020**, 400, 123297.

[23] Zeng, H., Yang, B., Zhang, J., Zhu, H., Deng, J., Shi, Z., Zhou, S., Zhang, H., Cai, A., Deng, L. MnFe layered double hydroxides confined MnO_x for peroxymonosulfate activation: A novel manner for the selective production of singlet oxygen. *Environ. Pollut.* **2024**, 348, 123865.

[24] Yin, K., Shang, Y., Chen, D., Gao, B., Yue, Q., Xu, X. Redox potentials of pollutants determining the dominate oxidation pathways in manganese single-atom catalyst (Mn-SAC)/peroxymonosulfate system: Selective catalytic mechanisms for versatile pollutants. *Appl. Catal. B-Environ.* **2023**, 338, 123029.

[25] Zhang, L., Qi, J., Chen, W., Yang, X., Fang, Z., Li, J., Li, X., Lu, S., Wang, L. Constructing hollow multishelled microreactors with a nanoconfined microenvironment for ofloxacin degradation through peroxymonosulfate activation: Evolution of high-valence cobalt-oxo species. *Environ. Sci. Technol.* **2023**, 57, 16141-16151.

[26] Zhang, X., Liu, J., Zhang, H., Wan, Z., Li, J. Uncovering the pathway of peroxymonosulfate activation over $Co_{0.5}Zn_{0.5}O$ nanosheets for singlet oxygen generation: Performance and membrane application. *Appl. Catal. B-Environ.* **2023**, 327, 122429.

[27] Yin, C., Xia, Q., Zhou, J., Li, B., Guo, Y., Khan, A., Li, X., Xu, A. Direct electron transfer process-based peroxymonosulfate activation via surface labile oxygen over mullite oxide YMn_2O_5 for effective removal of bisphenol A. *Sep. Purif. Technol.* **2022**, 280, 119924.

[28] Zhao, J., Hu, X., Kong, L., Peng, X. UV irradiation induced simultaneous reduction of Cu(II) and degradation of EDTA in Cu(II)-EDTA in wastewater containing Cu(II)-EDTA. *J. Hazard. Mater.* **2024**, 465, 133131.

[29] Hassani, A., Scaria, J., Ghanbari, F., Nidheesh, P.V. Sulfate radicals-based advanced oxidation processes for the degradation of pharmaceuticals and personal care products: A review on relevant activation mechanisms, performance, and perspectives. *Environ. Res.* **2023**, 217, 114789.

[30] Li, H., Yuan, N., Qian, J., Pan, B. Mn_2O_3 as an Electron shuttle between peroxymonosulfate and organic pollutants: The dominant role of surface reactive Mn(IV) species. *Environ. Sci. Technol.* **2022**, 56, 4498-4506.

[31] Zong, Y., Guan, X., Xu, J., Feng, Y., Mao, Y., Xu, L., Chu, H., Wu, D. Unraveling the overlooked involvement of high-valent cobalt-oxo species generated from the cobalt(II)-activated peroxymonosulfate process. *Environ. Sci. Technol.* **2020**, 54, 16231-16239.

[32] Li, B., Liu, Y., Hu, K., Dai, Q., Chen, C., Duan, X., Wang, S., Wang, Y. Spin-regulated fenton-like catalysis for nonradical oxidation over metal oxide@carbon composites. *Adv. Funct. Mater.* **2024**, 34, 2401397.

[33] Wang, H., Gao, L., Xie, Y., Yu, G., Wang, Y. Clarification of the role of singlet oxygen for pollutant abatement during persulfate-based advanced oxidation processes: Co_3O_4@CNTs activated peroxymonosulfate as an example. *Water Res.* **2023**, 244, 120480.

[34] Gao, L., Guo, Y., Zhan, J., Yu, G., Wang, Y. Assessment of the validity of the quenching method for evaluating the role of reactive species in pollutant abatement during the

persulfate-based process. *Water Res.* **2022**, 221, 118730.

[35] Hassani, A., Eghbali, P., Mahdipour, F., Wacławek, S., Lin, K.-Y.A., Ghanbari, F. Insights into the synergistic role of photocatalytic activation of peroxymonosulfate by UVA-LED irradiation over $CoFe_2O_4$-rGO nanocomposite towards effective Bisphenol A degradation: Performance, mineralization, and activation mechanism. *Chem. Eng. J.* **2023**, 453, 139556.

[36] Xu, M., Li, J., Yan, Y., Zhao, X., Yan, J., Zhang, Y., Lai, B., Chen, X., Song, L. Catalytic degradation of sulfamethoxazole through peroxymonosulfate activated with expanded graphite loaded $CoFe_2O_4$ particles. *Chem. Eng. J.* **2019**, 369, 403-413.

[37] Anipsitakis, G.P., Dionysiou, D.D., Gonzalez, M.A. Cobalt-mediated activation of peroxymonosulfate and sulfate radical attack on phenolic compounds. Implications of chloride ions. *Environ. Sci. Technol.* **2006**, 40, 1000-1007.

[38] Li, X., Wen, X., Lang, J., Wei, Y., Miao, J., Zhang, X., Zhou, B., Long, M., Alvarez, P.J.J., Zhang, L. CoN_1O_2 single-atom catalyst for efficient peroxymonosulfate activation and selective cobalt(IV)=O generation. *Angew. Chem. Int. Ed.* **2023**, 62, e202303267.

[39] Zeng, H., Deng, L., Yang, L., Wu, H., Zhang, H., Zhou, C., Liu, B., Shi, Z. *Novel Prussian blue analogues@MXene nanocomposite as heterogeneous activator of peroxymonosulfate for the degradation of coumarin: The nonnegligible role of Lewis-acid sites on MXene*. *Chem. Eng. J.* **2021**, 416, 128071.

[40] Wu, Z., Wang, Y., Xiong, Z., Ao, Z., Pu, S., Yao, G., Lai, B. Core-shell magnetic Fe_3O_4@Zn/Co-ZIFs to activate peroxymonosulfate for highly efficient degradation of carbamazepine. *Appl. Catal. B-Environ.* **2020**, 277, 119136.

[41] Yang, Y., Banerjee, G., Brudvig, G.W., Kim, J.-H., Pignatello, J.J. Oxidation of organic compounds in water by unactivated peroxymonosulfate. *Environ. Sci. Technol.* **2018**, 52, 5911-5919.

[42] Wu, S., Yang, D., Zhou, Y., Zhou, H., Ai, S., Yang, Y., Wan, Z., Luo, L., Tang, L., Tsang, D.C.W. Simultaneous degradation of p-arsanilic acid and inorganic arsenic removal using M-rGO/PS Fenton-like system under neutral conditions. *J. Hazard. Mater.* **2020**, 399, 123032.

[43] Ye, Q., Wu, J., Wu, P., Wang, J., Niu, W., Yang, S., Chen, M., Rehman, S., Zhu, N. Enhancing peroxymonosulfate activation of Fe-Al layered double hydroxide by dissolved organic matter: Performance and mechanism. *Water Res.* **2020**, 185, 116246.

[44] Zhou, Y., Jiang, J., Gao, Y., Pang, S.-Y., Ma, J., Duan, J., Guo, Q., Li, J., Yang, Y. Oxidation of steroid estrogens by peroxymonosulfate (PMS) and effect of bromide and chloride ions: Kinetics, products, and modeling. *Water Res.* **2018**, 138, 56-66.

[45] Lin, K., Liu, W., Gan, J. Oxidative removal of Bisphenol A by manganese dioxide: Efficacy, products, and pathways. *Environ. Sci. Technol.* **2009**, 43, 3860-3864.

[46] Wang, L., Cheng, H. Birnessite (δ-MnO_2) mediated degradation of organoarsenic feed additive p-arsanilic acid. *Environ. Sci. Technol.* **2015**, 49, 3473-3481.

[47] Wang, Z., Fang, Y., Yang, Y., Qiu, B., Li, H. Vacancies-rich MOFs-derived magnetic CoFe encapsulated in N-doped carbon nanotubes as peroxymonosulfate activator for p-arsanilic acid removal. *Chem. Eng. J.* **2023**, 454, 140474.

Supporting Information

$Co_4(PW_9O_{34})_2$ Polyoxmetalate Cluster Intercalated in Layered Double Hydroxides as Catalyst for the Oxidation of *p*-Arsanilic Acid and Subsequent Immobilization of Arsenic-Containing Byproducts

Hanxuan Zeng[a], Wenfang Shi[a], Bufan Yang[a], Jing Deng[a], Jue Wang[b,*], Haojie Zhang[c]

a. Zhejiang Key Laboratory of Civil Engineering Structures & Disaster Prevention and Mitigation Technology, College of Civil Engineering, Zhejiang University of Technology, Hangzhou, 310023, P. R. China

b. College of Architecture and Energy Engineering, Wenzhou University of Technology, Wenzhou, 325000, P. R. China

c. Department of Environmental Engineering, Helmholtz Centre for Environmental Research-UFZ, Leipzig, 04318, Germany

*Corresponding author.

E-mail address: wangjue0119@hnu.edu.cn (J. Wang).

Texts: 6

Figures: 11

Tables: 4

Pages: 23 (including the cover page)

Text S1. Catalyst characterization

The morphologies and microstructures of the prepared samples were characterized by HR-TEM (JEOL, JEM-2100F, Japan) with 200 kV acceleration voltage. XRD of the materials were carried out at room temperature using X-ray diffract meter (Bruker, D8 Advance, Germany) employing Ni-filtered Cu Kα radiation at a scan rate (2θ) of 0.02 s^{-1}. FTIR of the samples were obtained using fourier transform infrared spectrometer (Thermo Fisher Scientific, Nicolet 6700, USA) with a range of 400-4000 cm^{-1}. The chemical compositions and states of the samples were determined using XPS assembled an ESCALAB 250 apparatus (Thermo Fisher Scientific, K-Alpha, USA) at 3×10^{-10} mbar using Al Kα X-ray beams (1486.6 eV). Radicals were identified by ESR spectroscopy (Bruker, ESP300E, Germany) operated at a 3514 G center field and a 9.85 GHz microwave frequency. 5,5-Dimethyl-1-pyrroline-N-oxide (DMPO) and 2,2,6,6-Tetramethylpiperidine 1-oxyl (TEMP) were used as the spin trap compound in the ESR analysis. To analyze the total contents of metals, samples were pretreated by microwave digestion (Anton Paar, Multiwave PRO, Austria), and then the concentrations of these metals were analyzed using an inductively coupled plasma-optical emission spectrometer (Agilent Technologies, ICP-OES 710, USA).

Text S2. Experimental procedures

All batch-type experiments were carried out in a 100 mL quartz reactor at a constant temperature (25 ℃±1 ℃). Typically, quantitative catalyst was added into 50 mL of *p*-ASA solution. After reaching adsorption/desorption equilibrium within 10 min, a certain amount of PMS was injected into the system to start the reaction. At a given time interval, water sample was withdrawn, filtered through a 0.22 μm membrane filter and quenched by 0.1 M $Na_2S_2O_3$ solution for residual concentration determination. 0.1 M H_2SO_4 and NaOH were used to adjust the solution pH instead of buffer solutions as buffer solutions tend to interact with catalysts. Effect of ions strength on the degradation of *p*-ASA were performed by adding corresponding substances into the solution beforehand. All the experiments were carried out at least twice. The relative standard deviations (RSD) for the different batches were usually less than 5%.

Text S3. Analytical methods

The residual concentration of targeted pollutant was determined by high-performance liquid chromatograph (Shimadzu, LC-20A, Japan) equipped with ZORBAX Eclipse XDB-C18 column (Agilent, 150×4.6 mm, i.d., 5 μm particle, USA) and VWD detector. Details of detection methods are summarized in Tab. S1. The concentration of As(III) and As(V) in solution were measured using atomic fluorescence spectrometer (Jitian, AFS-8220, China). TOC was measured by organic carbon analyzer (Shimadzu, TOC-L, Japan). The PMS concentration was determined using 2,2′-azino-bis (3-ethylbenzothiazoline-6-sulfonic acid) diammonium salt (ABTS) method. The intermediate products were identified by liquid chromatography-mass spectrometry-mass spectrometry (Agilent, 1290 series, USA).

Text S4. Probe-based kinetic model

The oxidation of PMS and the adsorption of LDH-CoPW to *p*-ASA and probes could be ignored. Therefore, the removal of *p*-ASA by the LDH-CoPW/PMS system can be described by Eq. (S1).

$$-\ln\frac{[p-\mathrm{ASA}]}{[p-\mathrm{ASA}]_0} = k_{SO_4^{\bullet-},p-\mathrm{ASA}}\int[SO_4^{\bullet-}]\,dt + k_{^{\bullet}OH,p-\mathrm{ASA}}\int[^{\bullet}OH]\,dt + k_{^1O_2,p-\mathrm{ASA}}\int[^1O_2]\,dt + k_{Co(IV)=O,p-\mathrm{ASA}}\int[Co(IV)=O]\,dt \quad (S1)$$

The RSs exposure (i.e., $\int[SO_4^{\bullet-}]\,dt$, $\int[^{\bullet}OH]\,dt$, $\int[^1O_2]\,dt$ and $\int[Co(IV)=O]\,dt$) were calculated using the ternary Eqs. (S2)-(S5) based on the abatement of ATZ, PMD, MTZ and PMSO by the LDH-CoPW/PMS system.

$$-\ln\frac{[\mathrm{ATZ}]}{[\mathrm{ATZ}]_0} = k_{SO_4^{\bullet-},\mathrm{ATZ}}\int[SO_4^{\bullet-}]\,dt + k_{^{\bullet}OH,\mathrm{ATZ}}\int[^{\bullet}OH]\,dt + k_{^1O_2,\mathrm{ATZ}}\int[^1O_2]\,dt + k_{Co(IV)=O,\mathrm{ATZ}}\int[Co(IV)=O]\,dt \quad (S2)$$

$$-\ln\frac{[\mathrm{PMD}]}{[\mathrm{PMD}]_0} = k_{SO_4^{\bullet-},\mathrm{PMD}}\int[SO_4^{\bullet-}]\,dt + k_{^{\bullet}OH,\mathrm{PMD}}\int[^{\bullet}OH]\,dt + k_{^1O_2,\mathrm{PMD}}\int[^1O_2]\,dt + k_{Co(IV)=O,\mathrm{PMD}}\int[Co(IV)=O]\,dt \quad (S3)$$

$$-\ln\frac{[\mathrm{MTZ}]}{[\mathrm{MTZ}]_0} = k_{SO_4^{\bullet-},\mathrm{MTZ}}\int[SO_4^{\bullet-}]\,dt + k_{^{\bullet}OH,\mathrm{MTZ}}\int[^{\bullet}OH]\,dt + k_{^1O_2,\mathrm{MTZ}}\int[^1O_2]\,dt + k_{Co(IV)=O,\mathrm{MTZ}}\int[Co(IV)=O]\,dt \quad (S4)$$

$$-\ln\frac{[\mathrm{PMSO}]}{[\mathrm{PMSO}]_0} = k_{SO_4^{\bullet-},\mathrm{PMSO}}\int[SO_4^{\bullet-}]\,dt + k_{^{\bullet}OH,\mathrm{PMSO}}\int[^{\bullet}OH]\,dt + k_{^1O_2,\mathrm{PMSO}}\int[^1O_2]\,dt + k_{Co(IV)=O,\mathrm{PMSO}}\int[Co(IV)=O]\,dt \quad (S5)$$

The second order rate constants of *p*-ASA, ATZ, PMD and MTZ with Co(IV)=O were determined by using competition kinetics method. PMSO was used as a reference compound because its rate constant with Co(IV)=O is already known ($k_{Co(IV)=O,PMSO}$ = 2.00×10^6 M^{-1} s^{-1}). Co(IV)=O was generated in the Co^{2+}/PMS system at pH = 3.0 condition [1]. Of which, Co(IV)=O was the dominant species in this system and the contribution of other radical can be neglected. Probes and PMSO were simultaneously added into the Co^{2+}/PMS system (Fig. S6a and b). The second order rate constants of probes with Co(IV)=O can be calculated by Eq. (S6).

$$\frac{k_{probes}}{k_{Co(IV)=O,probes}} = \frac{k_{PMSO}}{k_{Co(IV)=O,PMSO}} \quad (S6)$$

Text S5. Transient concentration and contribution of reactive species

The transient concentration of $SO_4^{\bullet-}$, $^1O_2$ and Co(IV)=O were estimated by Eqs. (S7)-(S9) based on the ratios between $SO_4^{\bullet-}$ and PMS exposure ($R_{SO_4^{\bullet-}}$), $^1O_2$ and PMS exposure ($R_{^1O_2}$), Co(IV)=O and PMS exposure ($R_{Co(IV)=O}$)

$$R_{SO_4^{\bullet-}} = \frac{\int [SO_4^{\bullet-}]dt}{\int [PMS]dt} = \frac{SO_4^{\bullet-} \text{ concentration}}{\text{PMS concentration}} \quad (S7)$$

$$R_{^1O_2} = \frac{\int [^1O_2]dt}{\int [PMS]dt} = \frac{^1O_2 \text{ concentration}}{\text{PMS concentration}} \quad (S8)$$

$$R_{Co(IV)=O} = \frac{\int [Co(IV)=O]dt}{\int [PMS]dt} = \frac{Co(IV)=O \text{ concentration}}{\text{PMS concentration}} \quad (S9)$$

Based on the PMS and RSs exposure, the relative contribution of $SO_4^{\bullet-}$, $^1O_2$ and Co(IV)=O to the *p*-ASA degradation were calculated using Eqs. (S10)-(S12).

$$f_{SO_4^{\bullet-}} = \frac{k_{SO_4^{\bullet-},p-ASA} \int [SO_4^{\bullet-}]dt}{k_{SO_4^{\bullet-},p-ASA} \int [SO_4^{\bullet-}]dt + k_{^1O_2,p-ASA} \int [^1O_2]dt + k_{Co(IV)=O,p-ASA} \int [Co(IV)=O]dt} \quad (S10)$$

$$f_{^1O_2} = \frac{k_{^1O_2,p-ASA} \int [^1O_2]dt}{k_{SO_4^{\bullet-},p-ASA} \int [SO_4^{\bullet-}]dt + k_{^1O_2,p-ASA} \int [^1O_2]dt + k_{Co(IV)=O,p-ASA} \int [Co(IV)=O]dt} \quad (S11)$$

$$f_{Co(IV)=O} = \frac{k_{Co(IV)=O,p-ASA} \int [Co(IV)=O]dt}{k_{SO_4^{\bullet-},p-ASA} \int [SO_4^{\bullet-}]dt + k_{^1O_2,p-ASA} \int [^1O_2]dt + k_{Co(IV)=O,p-ASA} \int [Co(IV)=O]dt} \quad (S12)$$

Text S6. Density functional theory (DFT) calculation

DFT calculations were conducted by the hybrid Becke-3-Lee Yang Parr (B3LYP) density functional method at the 6-311++G (3df, 3pd) level with Solvation Model Based on Density (SMD) model on a Gaussian 09 package. Fukui function, as a principal reactivity descriptors in DFT, is widely used to forecast the reactivity position of a molecule, and it can be calculated as follows:

Nucleophilic attack: $f_k^+ = q_k(\mathrm{N}) - q_k(\mathrm{N+1})$

Electrophilic attack: $f_k^- = q_k(\mathrm{N-1}) - q_k(\mathrm{N})$

Radical attack: $f_k^0 = (q_k(\mathrm{N-1}) - q_k(\mathrm{N+1}))/2$

where q_k represents the population of atom k in the *p*-ASA molecule.

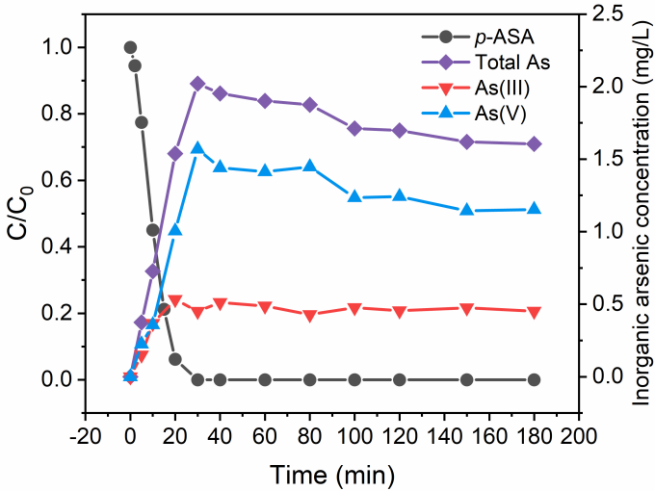

Figure S1. Variation of arsenic species concentration during reaction ([Catalyst] = 0.1 g/L, [PMS] = 0.1 mM, [*p*-ASA] = 10 mg/L).

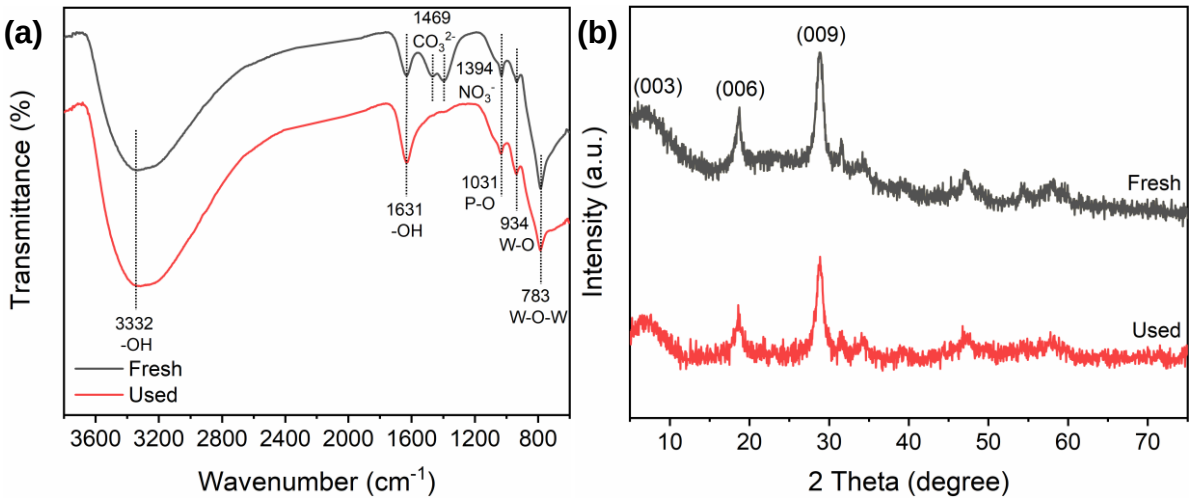

Figure S2. (a) FTIR and (b) XRD pattern of fresh and used LDH-CoPW.

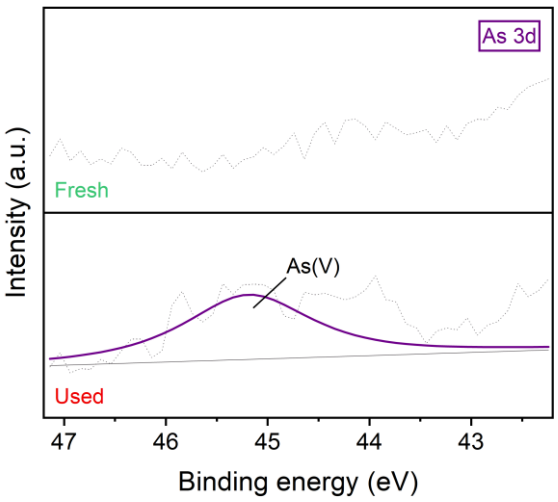

Figure S3. As 3d XPS spectra of fresh and used LDH-CoPW.

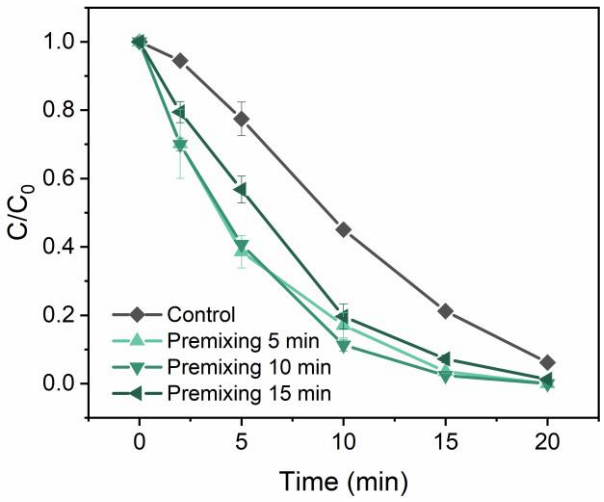

Figure S4. Effect of premixing time on *p*-ASA degradation in LDH-CoPW/PMS system ([Catalyst] = 0.1 g/L, [PMS] = 0.1 mM, [*p*-ASA] = 10 mg/L).

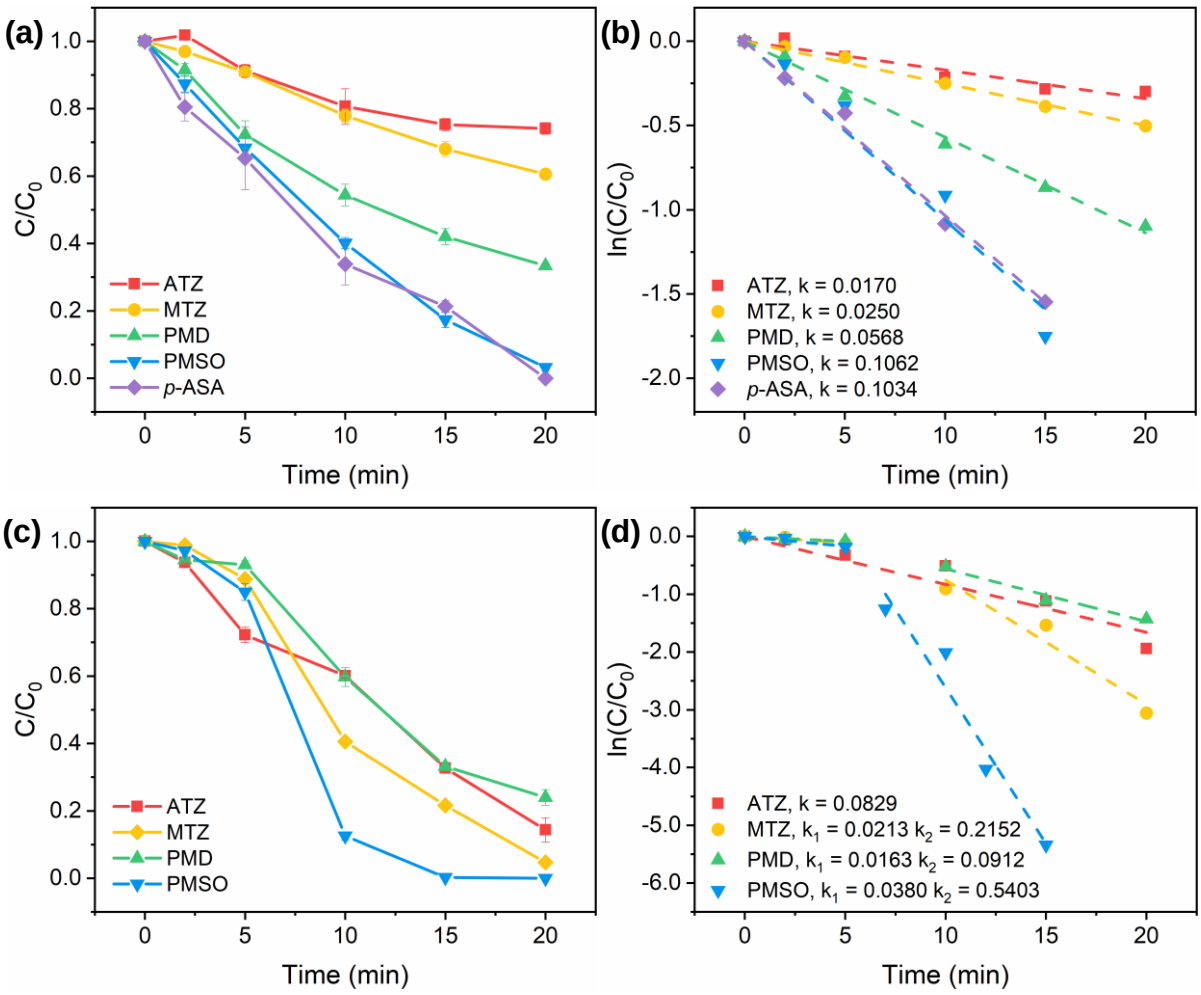

Figure S5. (a) Performance and (b) correlation coefficient of probe compounds degraded by Co(IV)=O; (c) Performance and (d) correlation coefficient of probe compounds degraded in LDH-CoPW/PMS system ([Catalyst] = 0.1 g/L, [PMS] = 0.1 mM, [Probes] = 1 mg/L).

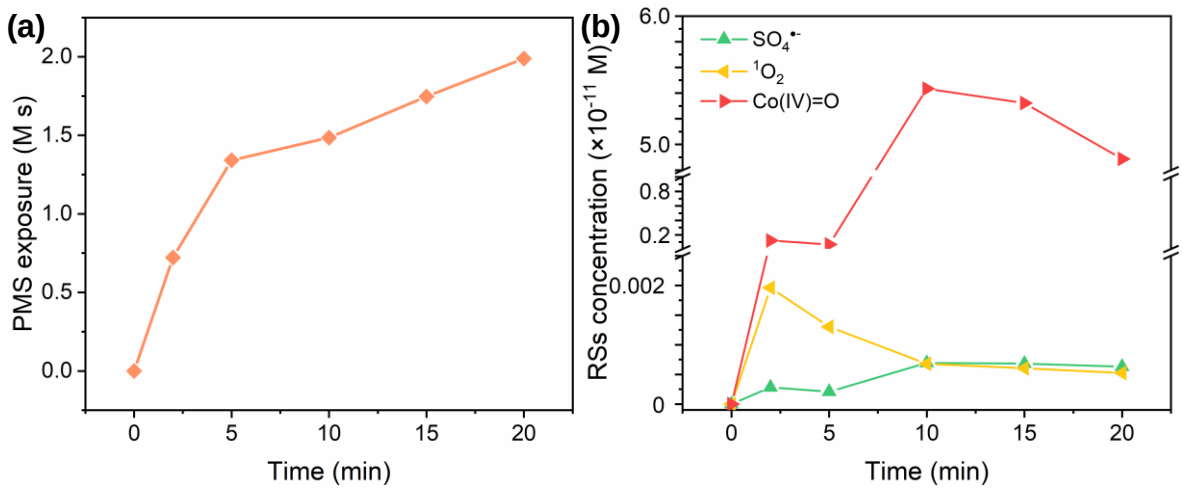

Figure S6. (a) PMS exposure; (b) Transient concentration of different RSs ([Catalyst] = 0.1 g/L, [PMS] = 0.1 mM, [*p*-ASA] = 10 mg/L).

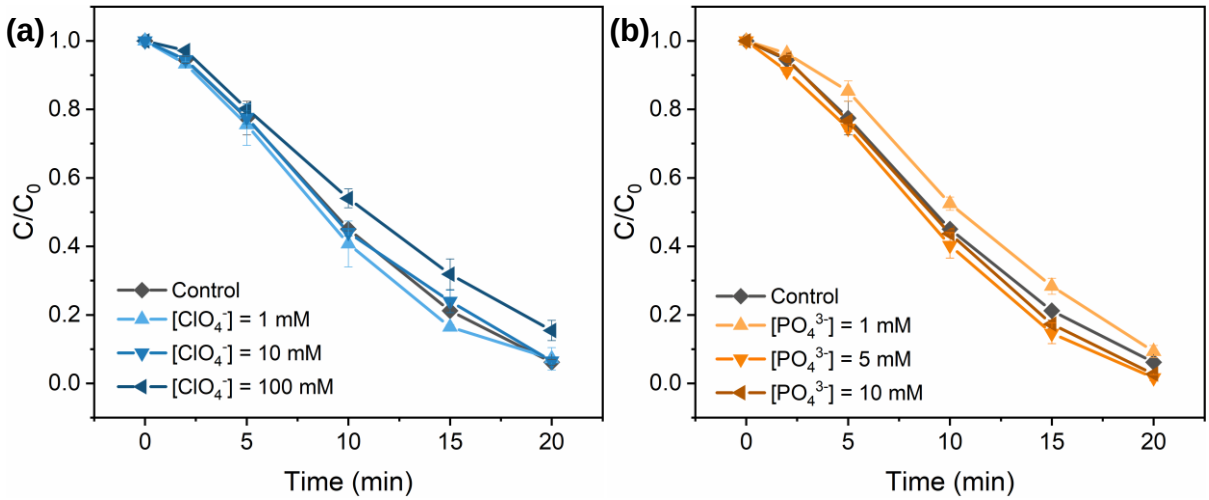

Figure S7. Effect of (a) ClO_4^- and (b) PO_4^{3-} on *p*-ASA degradation in LDH-CoPW/PMS system ([Catalyst] = 0.1 g/L, [PMS] = 0.1 mM, [*p*-ASA] = 10 mg/L).

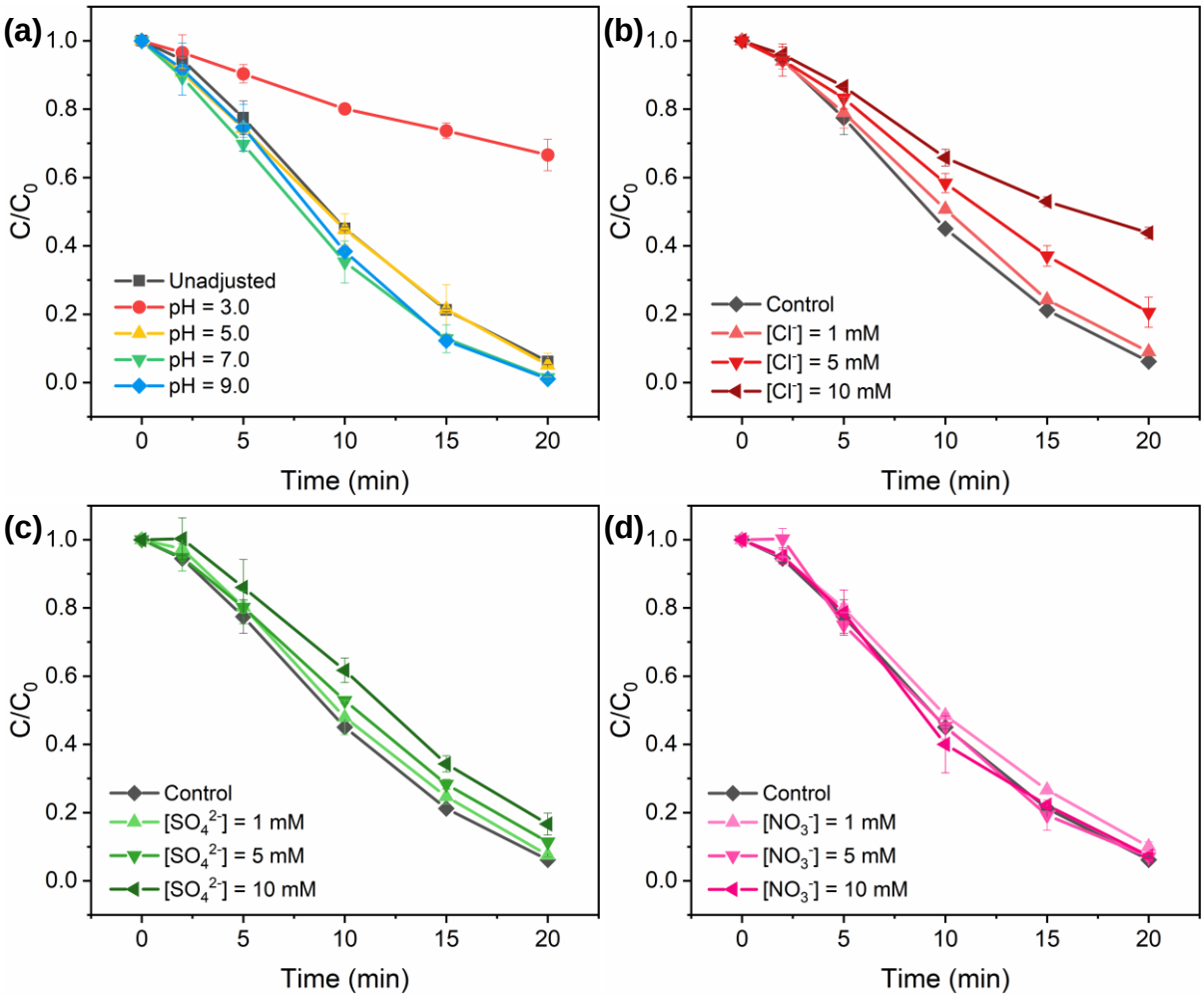

Figure S8. Effect of (a) initial pH, (b) Cl^-, (c) SO_4^{2-} and (d) NO_3^- on *p*-ASA degradation in LDH-CoPW/PMS system ([Catalyst] = 0.1 g/L, [PMS] = 0.1 mM, [*p*-ASA] = 10 mg/L).

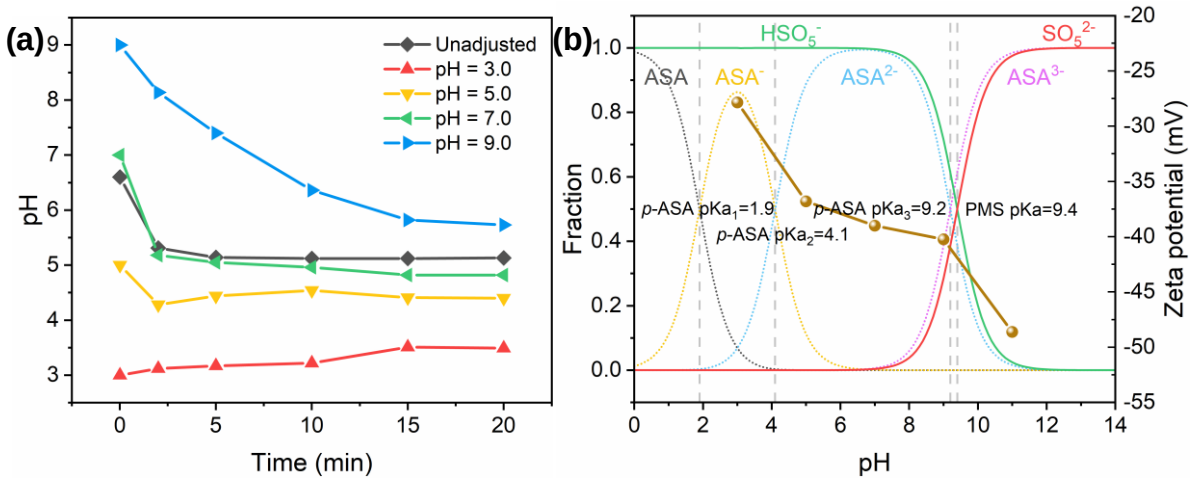

Figure S9. (a) pH values variation during the reaction; (b) Zeta potential of LDH-CoPW, the speciation of PMS and *p*-ASA.

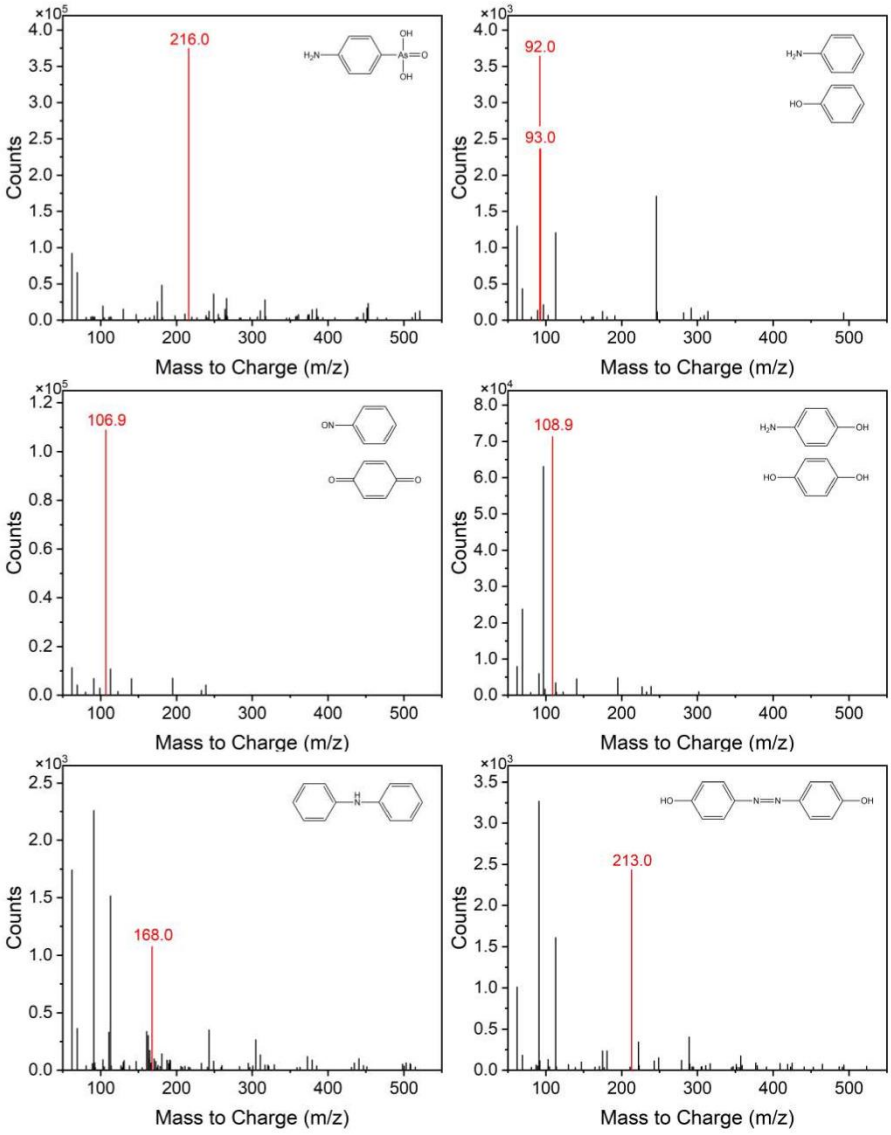

Figure S10. *p*-ASA and its degradation intermediates detected by LC-MS.

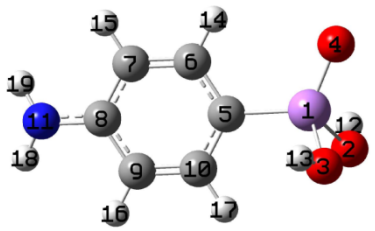

Atom	q(N)	q(N+1)	q(N-1)	f^-	f^+	f^0	CDD
1(As)	0.6033	0.5056	0.6498	0.0465	0.0977	**0.0721**	0.0512
2(O)	-0.2855	-0.3327	-0.2426	0.0429	0.0472	0.045	0.0043
3(O)	-0.2831	-0.3313	-0.2417	0.0414	0.0482	0.0448	0.0067
4(O)	-0.4462	-0.5172	-0.34	0.1062	0.071	0.0886	-0.0352
5(C)	-0.0955	-0.1608	-0.0121	0.0834	0.0653	**0.0744**	-0.0181
6(C)	-0.027	-0.0844	0.0128	0.0397	0.0575	0.0486	0.0177
7(C)	-0.0629	-0.1166	0.007	0.0699	0.0537	0.0618	-0.0162
8(C)	0.0617	-0.0357	0.1186	0.0569	0.0974	0.0772	0.0405
9(C)	-0.0626	-0.1064	0.0073	0.0699	0.0438	0.0568	-0.026
10(C)	-0.0299	-0.1096	0.0114	0.0413	0.0797	0.0605	0.0383
11(N)	-0.1589	-0.2207	-0.0196	**0.1393**	0.0617	**0.1005**	-0.0776
12(H)	0.1697	0.1427	0.187	0.0173	0.027	0.0221	0.0098
13(H)	0.1693	0.1431	0.1851	0.0158	0.0262	0.021	0.0104
14(H)	0.0537	0.0203	0.0819	0.0283	0.0333	0.0308	0.0051
15(H)	0.0426	0.0045	0.0791	0.0364	0.0381	0.0373	0.0017
16(H)	0.0422	0.0068	0.0787	0.0366	0.0354	0.036	-0.0012
17(H)	0.0528	0.0128	0.0827	0.0299	0.04	0.0349	0.01
18(H)	0.128	0.0902	0.1772	0.0491	0.0378	0.0435	-0.0113
19(H)	0.1283	0.0894	0.1774	0.0491	0.039	0.044	-0.0101

Figure S11. Natural population analysis (NPA) charge distribution and Fukui index of *p*-ASA.

Table S1. Analytic conditions of different organic compounds.

Name	Mobile phase		Wave length (nm)	Flow rate (mL/min)	Column temperature (℃)
p-ASA	Methanol 5%	0.1% formic acid 95%	255	0.8	40
ATZ	Methanol 70%	Water 30%	225		
MTZ	Acetonitrile 20%	Water 80%	318		
PMD	Methanol 50%	0.1% phosphoric acid 50%	218		
PMSO	Acetonitrile 20%	Water 80%	230	1.0	
$PMSO_2$	Acetonitrile 20%	Water 80%	215		

Table S2. Turnover frequency values of different catalysts in PMS activation.

Catalyst	Reaction conditions			Degradation performance			Ref.
	p-ASA (mg/L)	Catalyst (g/L)	Oxidant (mM)	Removal	k_{obs} (min^{-1})	TOF	
$CuFe_2O_4$	10	0.2	1	~85% (60 min)	0.03	0.015	[2]
pre-magnetized Fe^0	10	0.2	1	99% (30 min)	0.17	0.085	[3]
Co_3O_4-La_2CO_5@RSBC	10.8	0.2	0.3	100% (10 min)	0.18	0.273	[4]
LDH-CoPW	***10***	***0.1***	***0.1***	***93.8% (20 min)***	***0.09***	***0.9***	***This work***

Table S3. Second order reaction rate constants of probes with RS.

Probe	RS (M^{-1} s^{-1})			
	k $SO_4^{\bullet-}$	k $^{\bullet}OH$	k $^1O_2$	k Co(IV)=O
p-ASA	5.04×10^9 [5]	2.93×10^9 [6]	7.44×10^6 [7]	1.95×10^6 [*]
ATZ	2.60×10^9 [8]	3.00×10^9 [8]	4.00×10^4 [8]	3.20×10^5 [*]
MTZ	2.74×10^9 [9]	3.54×10^9 [9]	3.40×10^8 [10]	4.71×10^5 [*]
PMD	5.30×10^8 [8]	6.70×10^9 [8]	7.31×10^5 [8]	1.07×10^6 [*]
PMSO	3.17×10^8 [11]	3.61×10^9 [11]	No reaction	2.00×10^6 [1]

*determined in this study.

Table S4. Peaks information of Co 2p and Fe 2p.

Element	Valence		Binding energy	Relative ratio	
				Fresh	Used
Co 2p	Co $2p_{3/2}$	Co(III)	780.8 eV	62.7%	59.4%
		Co(II)	784.9 eV	37.3%	40.6%
Fe 2p	Fe $2p_{3/2}$	Fe(III)	712.2 eV	31.6%	32.2%
		Fe(II)	710.0 eV	68.4%	67.8%

References

[1] Zong, Y., Guan, X., Xu, J., Feng, Y., Mao, Y., Xu, L., Chu, H., Wu, D. Unraveling the overlooked involvement of high-valent cobalt-oxo species generated from the cobalt(II)-activated peroxymonosulfate process. *Environ. Sci. Technol.* **2020**, 54, 16231-16239.

[2] Chen, S., Deng, J., Ye, C., Xu, C., Huai, L., Li, J., Li, X. Simultaneous removal of para-arsanilic acid and the released inorganic arsenic species by $CuFe_2O_4$ activated peroxymonosulfate process. *Sci. Total Environ.* **2020**, 742, 140587.

[3] Chen, S., Deng, J., Ye, C., Xu, C., Huai, L., Ling, X., Li, J., Li, X. Degradation of p-arsanilic acid by pre-magnetized Fe^0/persulfate system: Kinetics, mechanism, degradation pathways and DBPs formation during subsequent chlorination. *Chem. Eng. J.* **2021**, 410, 128435.

[4] Li, Y., Liu, L., Wang, Z., Zhou, L., Lan, Y., Chen, C. Simultaneous oxidation of 4-aminophenylarsonic acid and adsorption of the produced inorganic arsenic by a combination of Co_3O_4-La2CO_5@RSBC with peroxymonosulfate. *Chem. Eng. J.* **2021**, 413, 127417.

[5] Gao, Y., Luo, Y., Pan, Z., Zeng, Z., Fan, W., Hu, J., Zhang, Z., Ma, J., Zhou, Y., Ma, J. Comparative study of Fe(II)/sulfite, Fe(II)/PDS and Fe(II)/PMS for p-arsanilic acid treatment: Efficient organic arsenic degradation and contrasting total arsenic removal. *Water Res.* **2024**, 249, 120967.

[6] Yang, T., An, L., Zeng, G., Jiang, M., Li, J., Liu, C., Jia, J., Ma, J. Efficient removal of p-arsanilic acid and arsenite by Fe (II)/peracetic acid (Fe (II)/PAA) and PAA processes. *Water Res.* **2023**, 241, 120091.

[7] Tyutereva, Y.E., Sherin, P.S., Parkhats, M.V., Liu, Z., Xu, J., Wu, F., Plyusnin, V.F., Pozdnyakov, I.P. New insights into mechanism of direct UV photolysis of p-arsanilic acid. *Chemosphere.* **2019**, 220, 574-581.

[8] Gao, L., Guo, Y., Zhan, J., Yu, G., Wang, Y. Assessment of the validity of the quenching method for evaluating the role of reactive species in pollutant abatement during the persulfate-based process. *Water Res.* **2022**, 221, 118730.

[9] Lian, L., Yao, B., Hou, S., Fang, J., Yan, S., Song, W. Kinetic study of hydroxyl and sulfate radical-mediated oxidation of pharmaceuticals in wastewater effluents. *Environ. Sci. Technol.* **2017**, 51, 2954-2962.

[10] Guo, Y., Long, J., Huang, J., Yu, G., Wang, Y. Can the commonly used quenching method really evaluate the role of reactive oxygen species in pollutant abatement during catalytic ozonation? *Water Res.* **2022**, 215, 118275.

[11] Wang, Z., Jiang, J., Pang, S., Zhou, Y., Guan, C., Gao, Y., Li, J., Yang, Y., Qiu, W., Jiang, C. Is sulfate radical really generated from peroxydisulfate activated by iron (II) for environmental decontamination? *Environ. Sci. Technol.* **2018**, 52, 11276-11284.